

Review

Not peer-reviewed version

A Review on Rubidium Two-Photon Vapor Cell Optical Clock: Long-Term Performance Limitations and Potential Improvements

[Asagwegbe C. Obaze-Adeleke](#) , [Bryan Semon](#) , [Thejesh N. Bandi](#) *

Posted Date: 30 April 2025

doi: 10.20944/preprints202504.2539.v1

Keywords: Vapor Cell Optical Clock; Rubidium optical clock; Long-term stability; Light Shift; Two-photon transition; Two-color two-photon transition






Preprints.org is a free multidisciplinary platform providing preprint service that is dedicated to making early versions of research outputs permanently available and citable. Preprints posted at Preprints.org appear in Web of Science, Crossref, Google Scholar, Scilit, Europe PMC.

Copyright: This open access article is published under a Creative Commons CC BY 4.0 license, which permit the free download, distribution, and reuse, provided that the author and preprint are cited in any reuse.

Review

A Review on Rubidium Two-Photon Vapor Cell Optical Clock: Long-Term Performance Limitations and Potential Improvements

Asagwegbe C. Obaze-Adeleke ¹, Bryan Semon ¹ and Thejesh N. Bandi ^{1,2,*}

¹ Department of Physics and Astronomy, College of Arts and Sciences, The University of Alabama, Tuscaloosa, AL 35401, USA

² Associate, Time and Frequency Division, National Institute of Standards and Technology, Boulder, CO 80305, USA

* Correspondence: tbandi@ua.edu

Abstract: Two-photon vapor cell based optical clocks are strong candidates for next-generation portable atomic standards, offering simplicity, compactness, and high performance. Their narrow clock transitions with counter-propagating beams enable first-order Doppler-free operation. However, systematic perturbations such as the AC Stark shift, temperature-induced shift, and drifts resulting from the laser system pose challenges, causing instabilities to the medium to long-term performances. This paper provides a comprehensive overview of Rb two-photon vapor cell optical standards, focusing on the long-term performance-limiting effects and potential mitigation strategies, aiming for clock stabilities better than 1×10^{-15} over the averaging time of a day and beyond.

Keywords: two-photon transition; vapor cell optical clock; rubidium optical clock; cesium two-photon vapor cell; long-term stability; light shift

1. Introduction

The breakthrough that led to atomic timekeeping dates back to 1945 when physicist Isador I. Rabi first suggested that scientists could use the oscillations of atoms to create precise clocks using atomic beam resonance [1–4]. Since then, scientists have developed various types of atomic clocks, continuously improving their performance and stability, advancing the world from the precision of microwave frequency standards (on the order of 10^{-16}) [5,6] to the unprecedented accuracy of optical frequency standards (reaching 10^{-19}) [7]. This level of precision corresponds to a loss of one second every 30 billion years [8]. Building upon these advancements, researchers have developed several cutting-edge optical clock technologies, including lattice- [9–25] and ion-based [26–35] clocks from atoms such as strontium, ytterbium, calcium, mercury and aluminum. Others include the sophisticated Nuclear clock built from thorium (^{229}Th) isomer [36–39], emerging hydrogen-based lattice clocks [40–44], clocks based on rapidly rotating neutron stars (known as millisecond pulsars) [45–50], molecular optical clocks [51] (including vibrational molecular clocks) [52,53], molecular iodine optical clocks [54–56], and molecular lattice clocks [57] (such as chip-scale molecular clocks) [58,59].

Advances in optical frequency combs [60–62], sophisticated laser systems, laser stabilization techniques, laser cooling and trapping of atoms and ions [63,64], and improved detection schemes have driven this significant experimental breakthrough in timekeeping, communication, satellite navigation [65,66], geodesy, deep space navigation, dark matter detection [67], and tests of fundamental physics [68], including the relativistic effects on timekeeping at the sub-millimeter scale. Due to rapid advancements in the unprecedented performance of optical clocks, the redefinition of the SI second is also being considered [8,65,66,69–77].

Numerous review papers and publications have extensively surveyed various aspects of timekeeping, including but not limited to the optical atomic clocks by Ludlow et al. [78], chip-scale atomic

devices by John Kitching [79], coherent population trapping in laser spectroscopy by Arimondo [80] and its advances by Vishal Shah and John Kitching [81], a review on atomic time, clocks, and clock comparisons in relativistic spacetime [82], pulsed optically pumped vapor cell frequency standards [83–97], and microfabricated atomic clocks [98–108].

As optical clocks advance as the leading frequency standards, researchers have focused on their miniaturization [63,109,110] for more compact, transportable, and out-of-the-lab use [11,111–113]. While neutral atom and ion-based optical clocks continue to set performance benchmarks in laboratory settings, simpler architectures—such as two-photon transitions in warm rubidium vapor cells [109,110,114–122]—offer promising paths toward compact and robust systems. To our knowledge, two companies currently lead the miniaturization of Rb vapor cell optical clocks, offering commercially available products: The Tiqker Rb Optical Clock by Inflektion, which demonstrates a maser-like short-term stability performance, and the Tempo Rubidium Optical Clock by QuantX Lab, which achieves a stability performance of 3×10^{-15} at 10000 s [123]. The Tiqker Rb optical clock is a 3U rack panel clock based on a hot-atom vapor-cell-based clock, weighing about 50 kg, providing a long-term frequency stability of $< 5 \times 10^{-15}$ [124]. The QuantX Labs Tempo Compact Rb optical clock is a 4U rackmount product weighing about the same (50 kg), with a patented optical interrogation system with $< 3 \times 10^{-15}$ at 10,000 s [123].

This work reviews the working principle of the Rb two-photon vapor cell optical clock, discussing the various challenges that impact its medium to long-term stability. Among these, we emphasize the light shift (AC Stark) effect due to its profound impact on the long-term performance of vapor cell optical clocks. Light shifts caused by the interaction of the atoms with the laser light can lead to significant frequency deviations, which are critical in applications requiring high precision over extended periods. We focus on understanding and mitigating the light shift alongside other factors, such as temperature variation shift, the instability contributions of the laser system, cell type, and detection methods. Effectively addressing the light shift is paramount as it not only enhances the stability of the clock but also significantly reduces the long-term drift in accuracy, which is estimated to be 5×10^{-11} per month and 5×10^{-10} per year [125]. Therefore, mitigating this effect is essential for advancing the reliability and utility of vapor cell clocks in practical applications [126–128].

This work is structured as follows: in section 2, we briefly describe the two-photon excitation principle; in section 3, we highlight the conventional vapor cell optical clocks with comprehensive discussion of the Rb two-photon optical clock principle and experimental procedure, including the key differences in the methods used by various authors and tables comparing various experimental parameters, as well as the comparison and drawbacks of the single and two-color scheme—additionally, we briefly summarize the cesium two-photon vapor cell optical frequency standards; in section 4, we briefly describe the short-term performance limiting effect, with greater emphasis being placed on the long-term performance limiting effect in section 5; section 6 discusses other performance-limiting effects; section 7 highlights various methods of suppressing light shifts and temperature-induced shifts in two-photon vapor cell standards; section 8 presents the conclusions and prospects.

2. Two-Photon Excitation Principle in Vapor Cell Optical Clocks

The theory of two-photon excitation was developed by Goppert-Mayer in 1931 using Dirac's dispersion theory [129,130]. Nearly four decades later (in the 1970s), Bernard Cagnac proposed the method of Doppler-free two-photon spectroscopy, which was first demonstrated in sodium atoms and then used extensively to study hydrogen atoms and measure the Rydberg constant and the Lamb shifts [130]. In 1962, Abella observed and reported the first two-photon absorption in the optical domain using cesium vapor atoms in an atomic excitation of the $6S_{1/2} - 9D_{3/2}$ transition in Cs using a pulsed ruby source at 653.55 nm [130–132]. However, with the advent of laser systems, increased power, and the reduction of linewidth techniques, scientists could use two-photon spectroscopy to make absolute measurements of atomic energy levels [130].

In a two-photon transition excitation scheme, the two photons, either at the same or at different wavelengths, combine their energies, matching the energy difference between the two states to drive transitions in an atom from a lower energy state to a higher energy state. The observance of a fluorescence signal determines the success of the two-photon excitation. The system generates an error signal, which corrects and locks the laser frequency to the atomic resonance. The quality and efficiency of the error signal depend on the laser field used in the excitation, the absorption cell, and the electronic control and measurement system [133].

3. Conventional Vapor Cell Optical Clocks

Portable optical clocks are revolutionizing precision metrology, satellite navigation, and quantum sensing by offering high stability and accuracy in compact, field-deployable systems. Among the most promising candidates for such clocks are optical transitions in alkali metals and simple molecules [109], which combine relative simplicity with advanced technological readiness. These systems leverage the straightforward energy-level structure [134] of alkali atoms, narrow spectral lines, and the ability to probe two-photon transitions using frequency-doubled fiber lasers [120,135]. They often operate without needing laser pre-stabilization, laser cooling, or ultra-high vacuum chambers. Their transitions are free from first-order Doppler-induced frequency shifts [117,119,132,135–140], which is around one hundred to one thousand times the natural linewidth [132]. Furthermore, the net momentum imparted to the atom during the transition is effectively zero, minimizing recoil effects and enhancing frequency stability [63,141]. Vapor cell based optical frequency standards are desirable due to their compact size and low cost compared to lattice optical frequency standards based on ions and cold atoms, which remain vastly complex and confined to laboratory settings [134,142]. As a result, vapor cell systems promise to enable transportable optical clocks [143] and novel applications in quantum technologies and beyond.

While this review concentrates on purely optical two-photon interrogation methods for rubidium and cesium vapor cell optical clocks, it is noteworthy that other techniques, such as coherent population trapping (CPT) [79,98,144–147] and pulsed optically pumped (POP) schemes [84–86,88–97], also offer significant advancements. These methods, extensively discussed in existing literature [80,81,147], present different advantages and challenges. For instance, researchers particularly value the CPT technique for its potential for miniaturization and low power consumption. However, it is limited by low signal contrast and stability compared to the two-photon optical technique [148,149]. Notably, a working linewidth of 9.3 kHz [149], 7.1 kHz [98], and 450 Hz [133] has been achieved in a chip-scale atomic clock using coherent population trapping (CPT). On the other hand, similar to the double resonance scheme [150–152], the POP schemes, which alternate between optical and microwave radiation, have been explored for their unique temporal separation of interactions, offering distinct benefits and drawbacks [91]. However, these alternative approaches are mentioned here for completeness and to contrast with the focus of our review, which remains on the potential and challenges of two-photon excitation in achieving high precision and stability in vapor cell clocks.

3.1. Rubidium Two-Photon Optical Clock

The rubidium gas cell atomic frequency standard is the most widely used portable atomic clock [4] for ground and space applications (e.g., Global Navigation Satellite Systems (GNSS)), primarily due to its low size, weight, power (SWaP), high stability, compact form factor, and suitability for a wide range of applications [153,154]. It has attracted significant interest, especially in the Rb two-photon vapor cell optical clock with a working linewidth of ≈ 330 kHz.

For Rb-87 atoms, the relevant transitions, as shown in Figure 1, are from the ground state $5S_{1/2}$ to the excited $5D_{5/2}$ state, with a cascade decay from the excited state to intermediate $6P_{3/2}$ state, and spontaneous decay to the ground state while emitting a blue fluorescence signal of 420 nm. The 420 nm clock signal is obtained from the cascade decay of $5D_{5/2}$ through $6P_{3/2}$ to $5S_{1/2}$. The observed

blue fluorescence signal increases linearly with atomic density until the gas becomes optically thick, and the gas reabsorbs the emitted blue light between the laser-defined excitation volume and the cell walls [137,155]. The $5D_{5/2}$ offers multiple decay channels, with the possibility of transitions to various intermediate states. The 420 nm fluorescence, while commonly used, is not the only option for fluorescence detection, nor does it possess the highest probability of occurrence [156] with an alternate detection scheme of 776 nm presented in [116].

Various experimental studies have reported the performance of Rb $5S_{1/2} - 5D_{5/2}$ two-photon optical clocks, reporting a long-term stability of 5×10^{-15} for an averaging time of 1 to 10 days [117], and a short-term stability of 1.5×10^{-13} at 1 s averaging time [122]. Despite these promising results, factors such as light shift variations (stemming from fluctuations in the laser optical power that probe the rubidium transition) [117,120,136,157], and vapor cell temperature variations [136] predominantly limit performance for medium-to-long averaging.

The natural linewidth of the two-photon transition in Rb is ≈ 330 kHz; however, as shown in Table 1, the measured linewidths consistently exceed this intrinsic value. Several factors primarily cause this broadening, such as transit-time broadening due to the finite interaction period of atoms with the laser and self-collisional broadening, as well as the laser's linewidth [158,159]. When the linewidth of the probing laser surpasses the intrinsic atomic linewidth, its contribution to the laser linewidth becomes significant, further broadening the observed linewidth.

In a recent comparative study on rubidium vapor cell, Perrella et al. [160] reported the atomic reference developed jointly by the Air Force Research Laboratory (AFRL) and the University of Adelaide. The AFRL approach employs two-photon single-color excitation and achieves a transition linewidth of 300 kHz, while Adelaide's two-color excitation clock yielded a degraded linewidth of 4 MHz because of the two colors employed. In theory, to achieve daily stability of typically 1×10^{-15} , the interrogating laser beam must be stabilized to 1 part per million (ppm) [119,156,161].

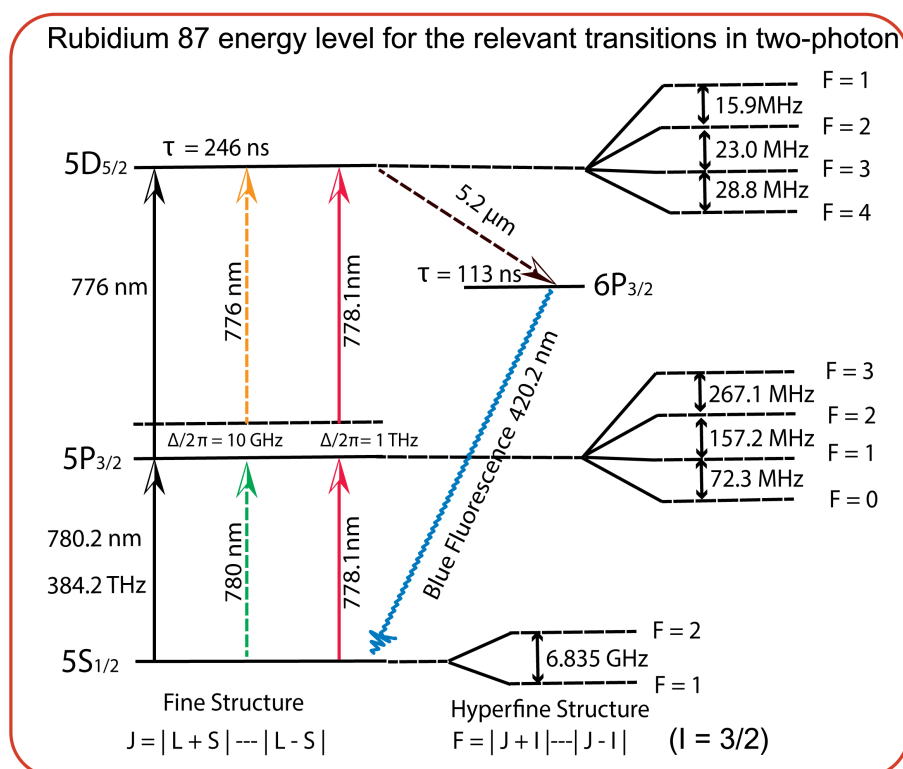


Figure 1. Rb-87 energy diagram, showing the fine and hyperfine energy splittings for two-photon excitation due to the identical (778.1 nm) and different wavelengths (780 nm + 776 nm). The natural linewidth of the Rb-87 transition is ≈ 330 kHz.

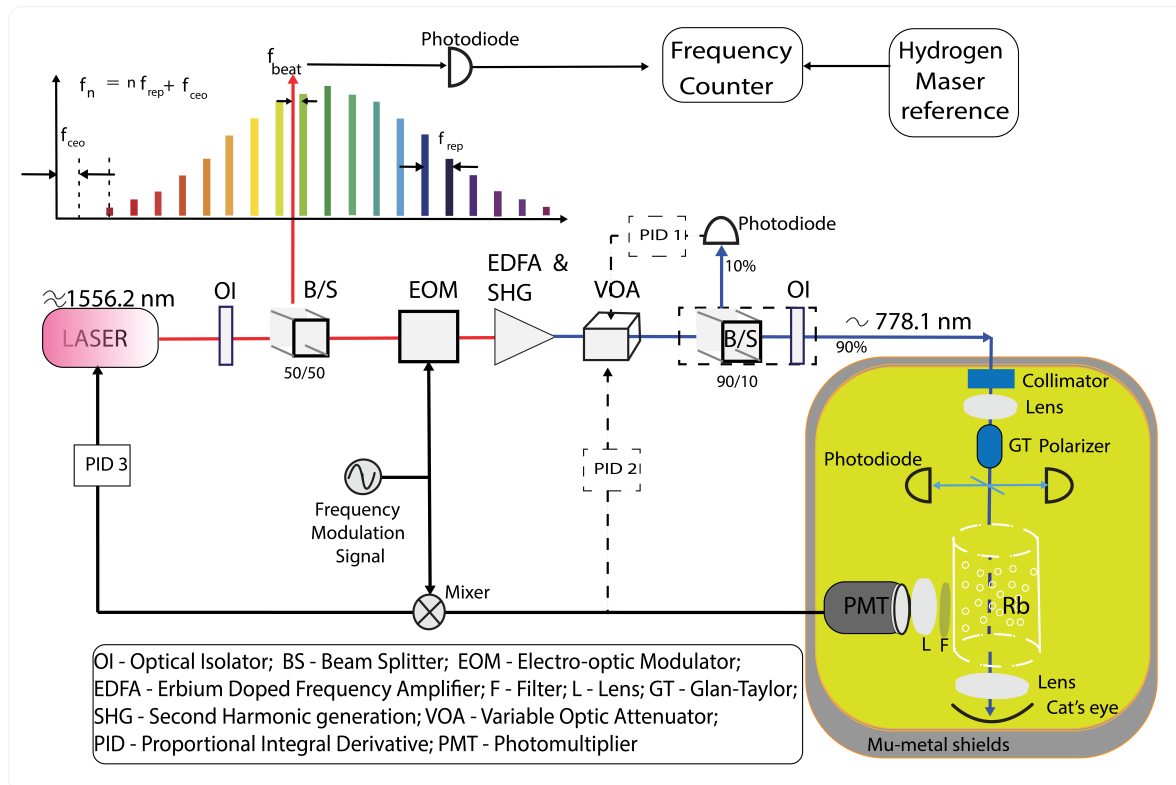


Figure 2. Generic scheme of two-photon single-color clock setup. The components with dotted lines are optional procedures. PID 1 and PID 2 are alternate methods of stabilizing the laser power. PID 3 is used for stabilizing the laser frequency. Further details of single-color schematics can be found in [109,110,114–120,161] and the experimental details on PID parameters optimization can be found in [162].

3.1.1. Two-Photon Single-Color Excitation

Experimentally, researchers implement this process using a tunable narrow linewidth laser, either operated at high power (40 - 70 mW) [120,163] or at low power [109,114,117,119], typically in the tens of milliwatt range. High power improves short-term stability by increasing atomic fluorescence. However, this improvement may come at the expense of degraded long-term frequency stability and increased drift unless the laser power stabilization is enhanced [117].

In place of a standard diode laser stabilized directly to the $5S_{1/2} - 5D_{5/2}$ two-photon transition of rubidium at 778 nm [71,109,130,163,164], second harmonic generation of telecom fiber lasers operating in the C-band around 1556 nm is used to generate 778.1 nm light [119,120,165]. This approach leverages the maturity of telecom laser technology, which offers well-established frequency stability, power stability, and long-term reliability. As shown in Figure 2, a typical free space optics or fiber-coupled setup is used with optical components such as isolators to prevent back reflection and formation of in-fiber etalons [117]. A portion of optical power is directed for amplification using an amplifier such as an erbium-doped frequency amplifier (EDFA) [62,119,166]. The free space setup offers flexibility but requires precise beam alignment of optical components. In contrast, the fiber-coupled setup minimizes the need to frequently fine-tune the alignment, thereby providing ease of use once aligned. However, challenges such as coupling efficiency and polarization drift persist, requiring tighter control [119]. Second harmonic generation (SHG) typically employs a nonlinear crystal selected according to application requirements such as the desired wavelength, available pump sources, nonlinear optical conversion efficiency, power output, linewidth, and operating temperature, [167] et cetera. The SHG is polarization sensitive [168]. Conventionally, a nonlinear periodically poled lithium niobate (PPLN) crystal is employed to frequency double the beam from 1556.2 nm to 778.1 nm as it has the advantage of a high nonlinear coefficient [167] and conversion efficiency around the rubidium transition with

only a minor susceptibility to the photo-refractive effect [169]. Hence, PPLN is an attractive option compared to other available SHG crystals, such as the Magnesium Oxide doped lithium niobate (MgO), Beta-Barium Borate (BBO), and periodically poled Potassium Titanyl Phosphate (PPKTP).

The rubidium cell maintained at a stable temperature between 80 - 100 °C receives the collimated and filtered 778.1 nm beam with the temperature efficiently controlled to avoid rubidium condensation at the cell windows of the cold spot [137]. It is often surrounded by mu-metallic shields to prevent stray magnetic fields from inducing an energy shift on the clock transition [163]. After passing the beam through a lens and a bandpass filter, a photodetector such as the commonly used photomultiplier tube (PMT) for the $6P_{3/2} - 5S_{1/2}$ transition [116,120,170] collects the 420 nm blue fluorescence signal. Other possible detectors include silicon photodetector [118], germanium photodetector [120], Hamamatsu H10721 – 110 PMT [171], a microfabricated PMT [110], and Hamamatsu S5972 photodiode [162]. In place of a 420 nm fluorescence, River et al. [116] reported the first collection of a 776 nm fluorescence in two-photon transition spectroscopy (Table 1). This novel approach demonstrated a 2.6-fold improvement in short-term instability compared to the conventional 420 nm fluorescence detection method [116]. As Martin [156] noted, fluorescence detection at 776 nm is an ideal choice for improving the signal-to-noise ratio. It does not have resonance with transitions involving the ground state, with zero radiation trapping of the fluorescence signal, and it has higher quantum efficiency and decay probability [156].

To retroreflect the beam through the Rb cell, which eliminates first-order Doppler-induced shift, a cat's eye [117,172] or a plane mirror [116,163] can be used to reflect the beam to pass through the cell by creating an anti-parallel beam [173]. To use a cat's eye, which is known to have a large acceptance angle and high accuracy [174], the dependence of the efficiency of the cat's eye on the angle of incidence must be calculated [175]. The detailed alignment calculations are in [156,172,176]. A simple geometrical alignment diagram for a flat mirror and a cat's eye is shown in [156,172], considering misalignment and its effects. As stated by Martin et al. [172], the cat's eye design minimizes the angular motion of retroreflector optics compared to a flat mirror. However, it poses sensitivity effects to the angular misalignment of the fiber launcher. Hence, the choice of retroreflector depends on the resolution and environmental conditions [174]. A flat mirror is preferable in a dynamic environment. In contrast, a cat's eye retroreflector is ideal for rigidly mounted collimators to reduce alignment variations [172].

While most applications employ single vapor cells (see Table 1 for possible dimensions) [109, 116,119,161,177], in principle researchers could use two vapor cells to double the laser's interaction length of the laser with the atomic vapor [117], albeit with a risk of increased etalon effect due to additional reflective surfaces. Properly orienting the vapor cell at an angle to the incident beam can minimize these effects [119,163]. The PMT output signal, proportional to the atomic fluorescence, is passed through a high-gain trans-impedance amplifier to enhance the signal, with an error signal generated from demodulating the PMT output [117]. This signal locks the laser frequency to the atomic clock transition. Factors such as laser power, modulation depth, modulation frequency, rubidium cell temperature [155], and pressure [178] determine the amplitude, slope, and shape of the laser frequency-locking error signal. In place of a PMT, a multi-pixel photon counter (MPPC) has proven effective in having high detection efficiency in the near-infrared wavelength [116]. To measure clock stability, a portion of the laser beam is directed to the frequency comb to convert the optical frequency into radio frequency for counting, referenced to a MASER clock. See [115,162] for frequency comb implementation.

3.1.2. Difference in Experimental Schemes

Experimental schemes in two-photon vapor cell optical clocks vary significantly across studies, reflecting diverse approaches to achieving stability and precision. Here, we present a summarized comparison of these schemes.

Poulin et al. [120] utilized a high-power multiple quantum well (MQW) distributed-feedback laser (70 mW) at 1556.2 nm with frequency doubling to probe the rubidium transition, achieving a fractional frequency instability of $5.8 \times 10^{-14} / \sqrt{\tau}$ for 100 seconds [120].

Zachary et al. [110] explored chip-scale atomic clocks using microresonator frequency combs for absolute clock transitions, achieving varied stabilities and demonstrating the use of dual-frequency combs for precise control [110].

Perrella et al. reported differences in linewidth and stability between single-color and two-color excitation schemes, highlighting the challenges of managing laser-induced broadening [160]

Maurice et al. [109]. developed a miniaturized optical reference using a microfabricated Rb vapor cell and in-line fluorescence detection, reaching a fractional frequency instability of $2.9 \times 10^{-12} / \sqrt{\tau}$ at 10^3 seconds averaging time [109].

Lemke et al. [117] conducted long-term measurements using a dual vapor cell setup, significantly reducing instabilities to 5×10^{-15} at 10 days averaging time [117].

Li et al. combined light shift and temperature compensation techniques in their two-photon clock, resulting in a notable reduction in frequency instability [161]. Although at the time of this review, this article is still in the arXiv preprint.

Beard et al. [116] introduced enhancements in emission line detection using a multi-pixel photon counter, leading to improved short-term instability metrics [116]

Erickson [115] used a direct comb excitation and reported the first observation of a residual Stark shift of $1.7834 \times 10^{-11} / \text{mW}$. The residual Stark effect is an inevitable shift in frequency observed in the AC Stark shift due to drift from the center wavelength of the frequency comb pulses and a change in spectral shape. This scheme achieved a comparable fractional light shift value of 7.6×10^{-12} , and a fractional frequency instability of $1.7 \times 10^{-13} / \sqrt{\tau}$

Each method has advantages and limitations, often dictated by the laser system, detection method, and specific vapor cell design. Table 1 comprehensively summarizes this two-photon single-color performance for detailed comparisons and technical specifications.

Table 1. Focuses on comparing the light shift value obtained in the Rb two-photon single-color optical scheme. We also show the experimentally reported values of the fractional frequency instability and a few other experimental parameters, such as the cell temperature and beam radius. The first observation of a 776 nm fluorescence is reported by Beard et al. [116] using a multi-pixel photon counter(MPPC) detector. However, the light shift value of the 420 nm fluorescence detection scheme is significantly better than that of the 776 nm fluorescence detection by over five orders of magnitude. The lowest value is demonstrated by Lemke et al. [117], with a total shift of -183 Hz for an input laser power of $10(1)$ mW. For the 776 nm fluorescence, a factor of 2.6 reduction in fractional frequency instability at an averaging time of about 100 seconds was observed, compared to other 420 nm detection schemes. The estimated fractional frequency at 1 s is with the assumption that the reported values will scale as $1/\sqrt{\tau}$ up to 1000 s; however, we note that this could be a best-case assumption. Additionally, Zachary et al. [110] also presented detailed characteristics of their standard in a [179]. Notably, the product from QuantX Labs known as the Tempo Compact Rb Optical Clock has shown a fractional frequency instability of 2×10^{-13} at 1 s, and reaching the stabilities down to 3×10^{-15} level at 10^4 s.

Articles	Signal Linewidth (kHz)	Cell Temperature (°C)	Vapor Cell Dimension (mm)	Beam Radius (μm)	Fractional Light Shift (per mW)	Reported Fractional Frequency Instability ($1/\sqrt{\tau}$)
Callejo et al. 2024 [114]	450	110	25 diameter, 70 length cell	100	-3.1×10^{-11}	3.5×10^{-13}
Erickson 2024 [171]	774	100	1/2" diameter, 1/2" length fill stem, 5 active length	230	7.6×10^{-12}	1.7×10^{-13}
Li et al. 2024 [161]	618	100	$N/R\ddagger$	800	$1.1 \times 10^{-12}\dagger$	$8.5 \times 10^{-14}\dagger$
Beard et al. 2024 [116]	N/R	106	5	490	-8.7×10^{-13}	2.12×10^{-13}
Lemke et al. 2022 [117]	550	100	50 diameter, 10 length	2100	-4.7×10^{-14}	5.0×10^{-13}
Maurice et al. 2020 [109]	2200	80	$N/R\ddagger$	Horizontal 200, Vertical 100	1.1×10^{-11}	2.9×10^{-12}
Zachary et al. 2019 [110]	1000	100	$3 \times 3 \times 3$	$N/R\ddagger$	-3.9×10^{-12}	4.4×10^{-12}
Gerginov et al. 2018 [118]	795	90	25 diameter, 25 length	400	$1.8(1\%) \times 10^{-13}$	$2.2 \times 10^{-15**}$
Martin et al. 2018 [119]	609	100	Rectangular prism of $5 \times 5 \times 25$	0.66(5)	4.8×10^{-13}	4.0×10^{-13}
Poulin et al. 2002 [120]	410	90	$N/R\ddagger$	420	-1.1×10^{-12}	2.5×10^{-13}

\dagger At the time of this review, it was only available at the arXiv preprint.

$**$ Estimated from spectroscopy.

\ddagger Not reported.

3.1.3. Two-Photon Two-Color Excitation

In the Two-color scheme, as shown in Figure 3, two lasers of different wavelengths (780 nm and 776 nm) are combined, with each laser tuned such that the sum of the photon energies corresponds to the Rb energy transition frequency with minimal detuning from the intermediate state. The frequency of the lasers f_{780} and f_{776} are locked to the nearest comb mode with mode number n_a and n_b to generate beat notes f_{b1} and f_{b2} , which is the difference between the laser frequency and the frequency of the comb mode ($[f_{780} - f_{na}, \text{ and } f_{776} - f_{nb}]$ respectively). f_{rep} represents the frequency repetition rate of the continuous train of pulses that forms the comb, while f_{ceo} is the carrier-envelope offset frequency of the comb. A wide range of 95 different detunings was previously measured by True et al. [180] for two-photon absorption rates in ^{87}Rb using two-color spectroscopy to examine the effects of polarization and detuning on the virtual intermediate state [180]. Hence, the two-photon

cross-section varied by more than six orders of magnitude across a 40 mm range of detunings with a clear dependence on polarization [180]. By taking advantage of the sign of the polarizability and maintaining the proper intensity ratio, the undesirable AC Stark shift [162] effect can be canceled. The overall contribution to the signal linewidth of such a standard is a contribution of the natural linewidth (≈ 667 kHz) and residual Doppler broadening [122].

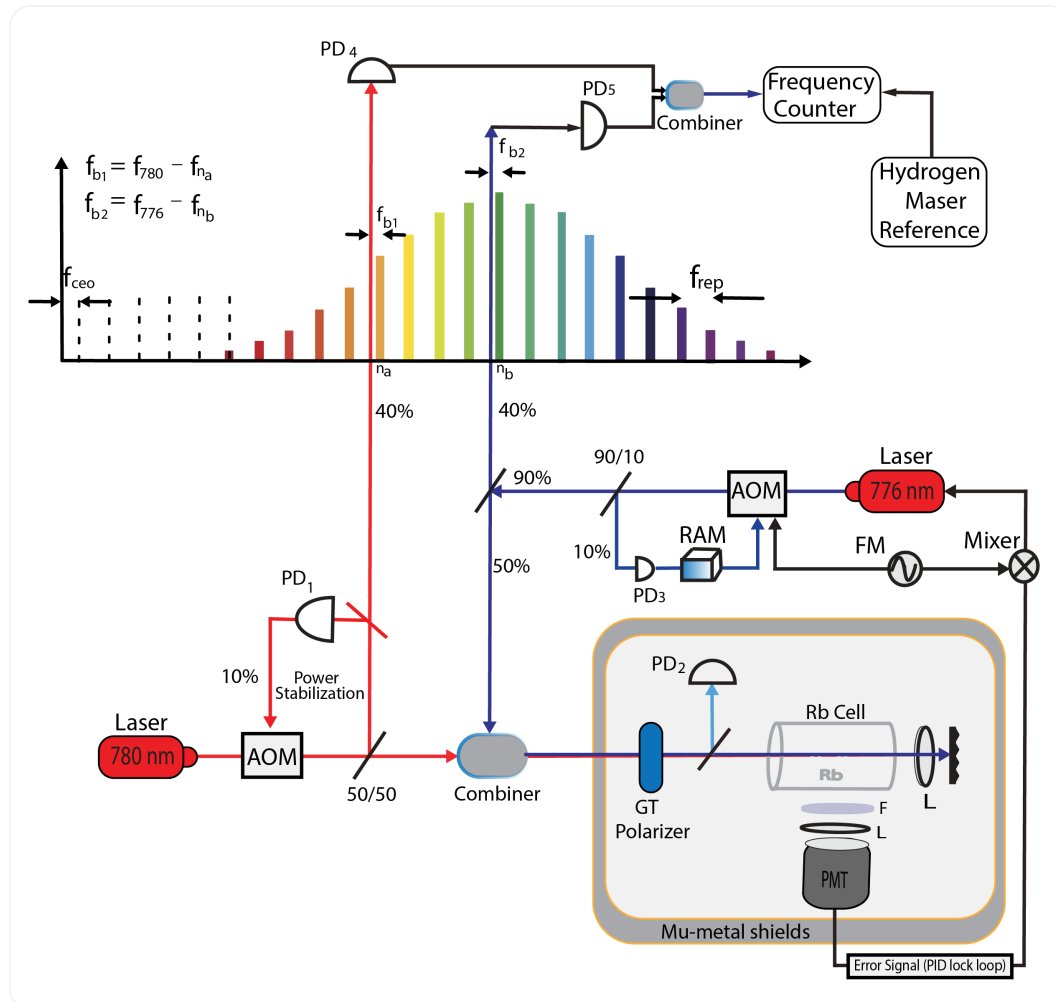


Figure 3. The general schematic of a two-photon two-color experimental setup. This involves combining two lasers of different wavelengths (780 nm and 776 nm) to interrogate the rubidium atoms. The intensities of the lasers are modulated using an acoustic optic modulator and combined before launching the linearly polarized beams into the cell containing the rubidium atoms. The 780 nm and 776 nm laser powers are generally stabilized using a feedback loop to the acousto-optic modulator (AOM) [122,181], or they can be directly stabilized to a frequency comb [118,121]. The AOM in the path of the 776 nm laser further serves the function of frequency modulation for locking and demodulating the error signal [182], as well as mitigation of the unwanted intensity modulation (RAM) resulting from the AOM [122,182]. The beat notes (f_{b1} and f_{b2}) generated from locking both lasers (780 nm and 776 nm) to the nearest comb tooth can be recorded using a frequency counter with the stability of the standard measured by comparing to a MASER clock, in this case, a hydrogen maser [121,122]. Alternatively, the frequency of the 780 nm laser can be stabilized using the saturation absorption spectroscopy method [183] to one of the sub-Doppler peaks of the Rb-87 D2 transition, while that of the 776 nm laser can be stabilized using the modulation transfer spectroscopy (MTS). AOM: Acousto-optic modulator; GT: Glan-Taylor; PD: Photodetector; F: Filter; L: Lens; PMT: Photomultiplier tube; RAM - Residual amplitude modulation; FM - Frequency modulation [118,121,122,136,177,181,182,184].

3.1.4. Experimental Schemes Discussion

This subsection briefly discusses the key differences in the experimental schemes employed by different authors.

The experimental schemes of Perrella et al. [122,160,181] demonstrate notable advancements in two-photon transition rates and frequency stability using different laser setups and detuning strategies. Initially, in 2013, they utilized an external cavity diode laser (ECDL) at 780 nm and a Ti:sapphire laser at 760 nm with slight detuning of 2 GHz from the intermediate state ($5P_{3/2}$), significantly enhancing the two-photon transition rate [181]. This setup used modulation transfer spectroscopy (MTS) for frequency stabilization, compensating for laser fluctuations and achieving a fractional frequency instability of 9.8×10^{-12} at 1.3 seconds [181]. In their 2019 scheme, two ECDLs were employed with a detuning of 1.5 GHz, achieving a 25-fold improvement in fractional frequency stability compared to a single-color scheme [122]. This scheme integrated three control loops for laser power and frequency stabilization, using photodiodes and acoustic-optic modulators to maintain precise control over the optical powers and frequencies. Furthermore, they controlled the sum of the two laser frequencies, resulting in a fractional frequency instability of 4.9×10^{-14} at 100 s [122].

On the other hand, Gerginov and Beloy [118] blue detuned their 780 nm wavelength by 10 GHz from the $5S_{1/2} - 5P_{3/2}$ [118]. The beams are combined and passed through a common AOM to be intensity-modulated at the same depth and afterward separated and recombined in the Rb cell in a counter-propagating configuration. The demodulated 780 nm beam, serving as a feedback signal, is locked to both the repetition rate of a frequency comb and the atomic transition [118]. A silicon photodetector was used for fluorescence collection because the detection efficiency is higher than a photomultiplier (PMT) [118]. Optical beam powers at $P_{780} = 1.2$ mW and $P_{776} = 19.2$ mW were used. From the spectroscopic measurements, the calculated value of the fractional frequency instability without considering the clock loop noise as reported is 0.3×10^{-15} at 1 second [118].

Nguyen and Schibli [136] proposed a two-color scheme similar to that of Gerginov and Beloy [118]. In their scheme, the 780 nm beam is red-detuned by 10 GHz from the $5S_{1/2} - 5P_{3/2}$, offering the possibility of operating the clock at a lower optimal temperature of 79.5 °C, which counters temperature-induced shifts and the AC Stark shift [136]. The drawback of this scheme is the dependence of the optimal temperature on the detuning of the 780 nm laser – necessitating the stabilization of the 780 nm laser to another laser probing the D2 transition $5S_{1/2} - 5P_{3/2}$, and locking the beat note either between this laser and the 10 GHz of the 780 nm, or by generating a single sideband of 10 GHz offset from the 780 nm probe laser and locking the sideband to the D2 transition [136]. Optical powers of $P_{780} = 1.2$ mW and $P_{776} = 16.93$ mW are needed to provide a power ratio of 0.0709 for the AC Stark shift cancellation to occur and the absolute power of each laser needs to be stabilized to 1.66×10^{-4} mW [136].

Hamilton et al. [177] combined two fiber lasers at 1552 nm and 1560 nm, amplified and frequency-doubled the beams to 776 nm and 780 nm, respectively, to excite the two-photon transition [177]. In this scheme, the 780 nm laser was detuned by 1.5 GHz using an electro-optic modulator (EOM) and stabilized using the saturation absorption spectroscopy technique [177]. For the 776 nm laser, they stabilized it to the $5S_{1/2} - 5D_{5/2}$ two-photon transition of rubidium using a feedback loop of the 420 nm clock signal obtained on a PMT [177]. The overall output of the clock was generated by the sum frequency of the 1552 nm and 1556 nm lasers, compared against a commercial frequency comb, pre-stabilized to an ultra-low expansion cavity [177]. They launched $P_{780} = 0.75(0.08)$ mW and $P_{776} = 1.2(0.1)$ mW into the cell, attaining a fractional frequency instability of 4×10^{-13} at 1 to 50 second integration time [177].

Finally, Ahern et al. [121] implemented a similar approach of combining two fiber lasers in a wavelength division multiplexer (WDM) at 1552 nm and 1560 nm, amplified using an EDFA and split into separate paths for individual modulation using an AOM, for second harmonic generation of 776 nm and 780 nm to drive the two-photon transition, with an intermediate state detuning of 1.5 GHz

[121]. The beams were stabilized using photodiodes, combined, and passed through a polarizer and optical wedge before launching into the rubidium cell (maintained between 60 - 70 °C) with a nominal power of ≈ 1 mW [121]. This scheme achieved the stability in the clock loop of 1.6×10^{-13} at $\tau = 1$ s and a value of 8.6×10^{-15} at $\tau = 2400$ s. Furthermore, they demonstrated the improved short-term performance, down to 6×10^{-14} at 1 s by detuning to 1.1 GHz and reducing the 780 and 776 nm laser powers, and a performance of 4.5×10^{-15} at $\tau = 2400$ s after removing residual fluctuation of the 780 nm laser power. [121]. Table 2 shows the summary of two-photon, two-color perturbative effects.

Table 2. Shows the experimentally reported values for the two-photon two-color rubidium optical clock scheme. While a few studies have shown the proof of concept and theoretical model for the two-color scheme, as seen from the table above, many experimental values are missing from the previous studies on such a scheme. There is a need for experimental measurement and characterization of the perturbing effects that threaten the medium to long-term performance of the clock. Hamilton Rhona et al., in their experimental and theoretical determination of polarizability alongside transition matrix elements in Rb-87, carried out a differential measurement of light shift. They found an experimental magic wavelength of 778.179(5) nm and a theoretical magic wavelength of 776.21 nm at the zero crossing of the polarizability [177]. Meanwhile, Nguyen and Schibli [136] proposed a two-color scheme that compensates for AC Stark shift, temperature-induced shift, and pressure-induced frequency shift for interrogating a rubidium vapor cell clock without trading off the Stark shift suppression. In their scheme, they red-detuned the 780 nm laser by 10 GHz for the D2 transition of Rb-87, thereby reducing the temperature-induced shift and allowing the clock to operate at a lower temperature. This enabled them to achieve a Rb-Rb collisional shift of -27 kHz/mTorr. While none of the authors reported a theoretical or experimental value for the light shift, Nguyen and Schibli calculated that a 1% power fluctuation in one of their laser diodes induced a fractional frequency shift of 1.8×10^{-13} [136]. This finding indicated that the beam power needs to be stabilized to a fractional level of 1.66×10^{-4} to achieve a noise floor of 3×10^{-15} at 100 s [136].

Category	Authors	Beam radius (μ m)	Laser Power (mW)	Detuning (GHz)	Signal Linewidth (kHz)	Fractional Frequency Instability	Light Shift (per mW)	Rb-Rb Shift (kHz)	Cell Temper- ature °C
Experimental studies	Ahern et al 2024 [121]	600	$P_{776} = 6.2,$ $P_{780} = 0.22$	1.5	340000	8.6×10^{-15} at $\tau = 2400$ s	-2.14×10^{-10} at 780 nm, 1.52×10^{-11} at 776 nm	N/R†	70
	Perrella et al. 2019 [122]	1500	$P_{776} = 1.2,$ $P_{780} = 0.75$	1.5	3470 ± 20	4.9×10^{-14} at $\tau = 10^2$ s	-10.90×10^{-10} at 780 nm, 1.17×10^{-10} at 776 nm	-1.82 ± 0.01	90
	Gerginov and Beloy 2018 [118]	2000	$P_{776} = 19.2,$ $P_{780} = 1.2$	10	3480	$0.3 \times 10^{-15}†$ at 1 s	$8.7(1\%) \times 10^{-14}$	N/R†	90
	Perrella et al. 2013 [181]	N/R†	$P_{776} = 0.004,$ $P_{780} = 0.003$	2	10400	5.9×10^{-12} at 10 s	1.40×10^{-6} at 780, 7.72×10^{-8} at 776 nm	-1.8 ± 0.7	90 ± 5
Theoretical studies	Rhona et al. 2023 [177]	1500	$P_{776} = 1.2,$ $P_{780} = 0.75$	1.5	667	4×10^{-13} for 50 s	N/R†	N/R†	80 ± 10
	Nguyen et al. 2022 [136]	1000	$P_{776} = 16.93,$ $P_{780} = 1.2$	0	N/R†	N/R†	N/R†	N/R†	79.5

† Estimated value from spectroscopy
‡ Not reported

3.2. Comparison and Drawbacks of the Single-Color and Two-Color Rb Schemes

While researchers have extensively investigated the single-color scheme because of its simplicity, the two-color excitation method presents several advantages. Recent progress has demonstrated that this two-color approach effectively minimizes the AC Stark shift, drawing growing attention from research. Despite these advancements, each scheme has its own set of drawbacks, explained as follows.

In the single-color scheme, a typical detuning of $\Delta \approx 1.1$ THz from the intermediate state is used. This approach, however, results in a relatively low two-photon transition rate, necessitating higher laser power to compensate and boost atomic fluorescence [122]. Unfortunately, this increase in intensity often leads to degraded long-term stability and increased drift, adding complexity to the system by requiring precise, tight control over laser power to maintain stability [117,122].

Unlike the single-color approach, the two-color scheme makes it possible to use less power and lower cell temperatures without compromising performance. In addition, this scheme provides flexibility in tuning the intermediate state and balancing the laser power [121]. Despite these advantages, it suffers from limitations, such as the manifestation of a Voigt profile — a convolution of Lorentian natural linewidth with a Doppler-broadened Gaussian profile — causing shifts in signal center frequency due to incomplete elimination of Doppler effects and broadening of the transition linewidth [121,122,162].

Experimental results, as detailed in Table 1 and 2, show that the two-color scheme (excluding spectroscopy measurements) has demonstrated excellent short-term stability of 1.5×10^{-13} , as reported by Perrella et al. [122] (also see Figure 5). In contrast, the best long-term stability demonstrated to date is attributed to the single-color scheme by Lemke et al., with a stability of 5.5×10^{-15} for a 10-day measurement period [117]. Notably, the single-color scheme effectively mitigates the long-term light shift perturbing effect, demonstrating the best value of light shift limitation at -4.7×10^{-14} , as reported by Lemke et al. [117]. As research efforts in two-color schemes continue to advance, researchers expect better long-term performance in the future.

3.3. Cesium Two-Photon Vapor Cell Optical Clock

While the primary focus of this review is on Rb two-photon vapor cell optical clocks, it is instructive to discuss the cesium (Cs) vapor cell optical clocks for comparative insights. Since their inception in 1967, *microwave* atomic clocks based on the ground-state hyperfine transition in ^{133}Cs have served as the primary frequency standards [65,143]. Here, we cover the Cs two-photon vapor cell *optical* clocks with features and practical advantages and their role in precision metrology.

Unique spectral properties of Cs atom gives an advantage for realizing high-performance optical clock. Among these, the $6S_{1/2} - 8S_{1/2}$ two-photon transition has been extensively studied using techniques like two-photon spectroscopy [185–193] and direct frequency comb spectroscopy [194,195]. This transition has a theoretical natural linewidth of 1.5 MHz [191], although there are reported theoretical narrower linewidths of 920 kHz for the same transition [187,195].

Notably, cesium has only one naturally stable isotope ^{133}Cs , eliminating complications arising from the spectral overlap of multiple isotopes [143,190]. It offers a practical advantage over other alkali metals — for instance, at the same cold-finger temperature, cesium vapor exhibits a higher atom density compared to other alkali metals (except francium), leading to a higher signal-to-noise ratio and, consequently, better clock stability [190]. Moreover, the $S - S$ transition in cesium is insensitive to the Earth's magnetic field due to the absence of the linear Zeeman effect for this transition, and the Zeeman shift scales quadratically with magnetic field at low field strength [190]. These features, combined with the long lifetime of the $6P_{3/2}$ state $\tau = 30.105(77)$ ns and the straightforward preparation of cesium vapor cells, suggest that the $6S - 6P$ D2 transition could serve as an excellent optical frequency reference [143].

Beyond its role in optical clocks, cesium-based systems have broader applications. For example, Shi et al. demonstrated that the high-performance laser sources derived from cesium optical clocks

can be integrated into optically pumped cesium beam atomic clocks to reduce laser frequency noise and improve the performance of microwave atomic clocks [143]. Caracas et al. [185] were the first to theoretically and experimentally investigate the $6S_{1/2} - 8S_{1/2}$ two-photon absorption cross section in hot cesium atoms. Using an external cavity diode laser (ECDL LP820P100) to drive the two-photon transition, they detected fluorescence signals from $7P_{1/2} - 6S_{1/2}$ and $7P_{3/2} - 6S_{1/2}$, using a Hamamatsu R5929 photomultiplier tube (PMT) for the two hyperfine transitions in cesium $F = 3 - F' = 3$ and $F = 4 - F' = 4$ [185].

This section briefly reviews the development and progress of two-photon cesium vapor-based optical clocks. We highlight the experimental advancements and compare the results across different schemes.

3.3.1. Experimental Procedure

The experimental setup for studying the cesium two-photon vapor cell optical clock typically employs an external cavity diode laser (ECDL) tuned to the specific transition wavelength of interest. The single isotope of Cs has various suitable transitions for realizing a standard. For the $6S - 8S$ two-photon transition in Cs, the appropriate laser wavelength is 822 nm. This transition is advantageous as it allows for the observation of blue fluorescence at 456 nm through a cascade decay from the $8S$ state followed by the $7S$ intermediate state to the $5S$ ground state [190,191].

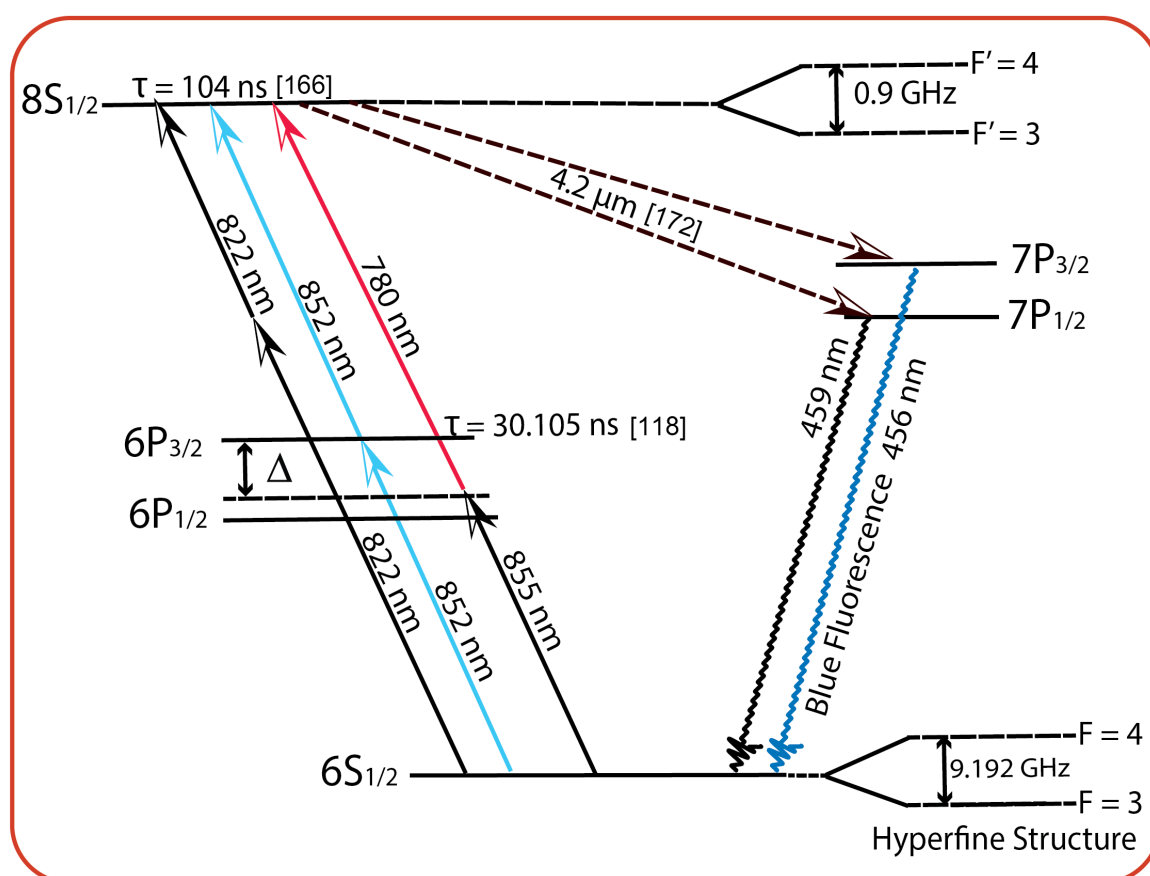


Figure 4. Shows the partial energy level diagram for two-photon transition in cesium. Fluorescence is readily observed from the $7P$ transition to the ground state. [143,185,191,193,195].

The Cs cell is typically enclosed within a Fabry-Perot cavity, which not only precisely defines the two-photon excitation geometry but also helps to effectively cancel the first-order Doppler effect, thereby enhancing the precision of frequency measurements [191]. To shield the experiment from

environmental magnetic fields, mu-metallic shields are often used around the cell. The primary transitions of interest for Cs two-photon vapor cell frequency standards include $6S_{1/2}(F = 4) - 6P_{3/2}(F' = 5)$; $6S_{1/2}(F = 4) - 6P_{3/2}(F' = 4)$. To stabilize the laser at these transitions, a laser operating at 852 nm is directly locked to the absorption lines of the Cs atoms [143,196]. It is noted in literature that factors contributing to linewidth broadening in these setups include not only transition line broadening but also the time of flight broadening due to the movement of cesium atoms within the cell [195]

In 2001, Masataka and Kazunori [197] used a mode-locked fiber laser to directly generate a pure 9.1926 GHz signal instead of using a multiplexer to change a 5 GHz quartz oscillator into 9.1926 GHz [197]. This was achieved by locking the repetition rate of a regenerative mode-locked fiber laser operating at 1.5 μm to the microwave 9.1926 GHz atomic resonance of Cs to realize a stable optical time clock [197]. From the error signal, their scheme simultaneously achieved a short-term stability of 7.1×10^{-12} for an averaging time of $\tau = 1$ s, and an ultrastable optical pulse train that is as stable as the Cs optical clock [197].

In 2011, Chen et al. [188] demonstrated high-resolution two-photon spectroscopy using a low-power external-cavity diode laser (ECDL) with an intracavity Cs cell. The authors investigated the lineshape symmetry, pressure shift, and potential interaction between the absorber (Cs cell) and laser cavity while demonstrating the system's application for laser stabilization. The Cs cell was maintained at (100°C) with temperature stability of 1 mK, using a single layer of mu-metal shielding to mitigate the effects of the Earth's magnetic field [188]. The study focused on three transition groups of ^{133}Cs at different wavelengths: $6S_{1/2} - 6D_{3/2}$ at 885.4 nm, $6S_{1/2} - 6D_{5/2}$ at 883.7 nm, 40 mW; and $6S_{1/2} - 8S_{1/2}$ at 822 nm, 100 mW. The intracavity approach offered several advantages, including a high-resolution spectrum that provides a good error signal for laser stabilization, minimal perturbation from the weakly induced quadrupole moment, and the elimination of Doppler background due to complete beam overlapping [188]. The authors achieved an improved signal-to-noise (SNR) by a factor of 10^2 compared to previous work [198], using less power by three orders of magnitude. This enhancement allowed them to resolve some previously unobserved spectral features, including the $F = 4 - F'' = 2$ and $F = 3 - F'' = 1$ transitions of the $6S_{1/2} - 6D_{5/2}$ state [188]. Without magnetic shielding, the linewidth of the $F = 4 - F'' = 6, D_{5/2}$ broadened by 1.2 MHz, and it should be noted that adding more layers of mu-metal did not further reduce the linewidth [188], proving that the broadening was not due to magnetic effects. The laser stabilization was achieved using two-hand-sized lasers stabilized to the $6S - 8S, F = 3 - F''' = 3$ transition [188]. The frequency instability was estimated from a beat note measurement between two independent lasers, yielding 3×10^{-13} at a 400 s sampling time [188]. However, it is important to note that they did not derive this instability from a traditional Allan deviation but used an estimated value due to the limitations of the lambda-type counter used in their experiment. The authors also measured the pressure shift (-290 kHz/Pa) and modulation shift (3 kHz/MHz) of the $6S - 8S$ transition, which are important for understanding the system's performance [188].

In 2013, Wu et al. [187] demonstrated a high-resolution method measuring the absolute frequency scheme of Cs $6S - 8S$ two-photon transition at 822 nm. The authors introduced an innovative experimental scheme that utilized two cesium cells, along with an electro-optical modulator (EOM) and an acousto-optic modulator (AOM). Cs cell one, maintained at 81°C and shielded with a single layer of mu-metal, was used in the Pound-Drever-Hall (PDH) laser stabilization and linewidth narrowing. Cs cell two, on the other hand, was employed to resolve the unperturbed two-photon transition spectrum of cesium. EOM and AOM were used to achieve three key objectives simultaneously: narrowing the laser linewidth, stabilizing the laser frequency using PDH locking, and resolving the transition spectrum by scanning the laser carrier frequency [187]. The experiment employed an ECDL as the master laser, whose output was amplified and spatially filtered to produce a 200 mW beam. They split the laser beam between an EOM – which they configured for frequency stabilization and scanning,

and an AOM – which was used to shift the laser carrier frequency to be in resonance with a specific spectral line for regulating the laser light intensity in the second cesium cell (Cs cell two) [187]. The entire system was self-referenced and monitored by a Ti:sapphire frequency comb laser, which was in turn referenced to a symmetricom 5071A cesium clock. They demonstrated the performance of 10^{-11} at 10 s averaging time, and 1.4×10^{-14} over one-day. The time bases of the EOM and AOM were phase-locked against the time base of the cesium clock, ensuring precise frequency control and stability throughout the experiment [187]. The authors inspected ten cesium cells to determine the accuracy of the transition frequency, with a particular focus on cells that exhibit a Lorentzian linewidth close to the theoretical natural linewidth (920 kHz). Their experiment demonstrated that the transition frequency obtained (364,507,238,000 kHz for $F = 3 - F' = 3$, and 364,503,080,000 kHz for $F = 4 - F' = 4$) from the cesium cell at room temperature using a single mu-metal is very close to the transition frequency for an ideal conditions of zero collision and zero magnetic fields [187]. While the authors provided a detailed error budget for a single cell and stability measurements for individual components (e.g., the laser and the cesium clock), the Allan deviation for the entire clock for the 6S – 8S transition was not explicitly reported.

Shi et al. [143] developed a dual-frequency optical-microwave standard that combines a cesium vapor cell for the optical clock and a Cs atomic beam for the microwave clock. This system allows for simultaneous operation or easy switching between the microwave and optical modes [143]. The optical cesium clock involves stabilizing the frequency of a homemade extended cavity diode laser (ECDL) operating at 45 mW and 852 nm wavelength to the $6S_{1/2}(F=4) - 6P_{3/2}(F' = 5)$ transition of hot Cs atoms using modulation transfer spectroscopy [143]. They maintained the cell temperature at 35°C, with a double-layer mu-metal magnetic shield. An optical frequency comb, referenced to a hydrogen maser, estimates the frequency stability of their Cs clock. The stabilized laser is then applied to an optically pumped cesium beam atomic clock, achieving the microwave clock frequency stability of 6×10^{-15} at 10^5 s to reduce the laser frequency noise. Notably, the Cs optical standard achieved a short-term performance of 3.9×10^{-13} at 1 s but degraded to 3.3×10^{-12} at 10^4 s. As reported by the authors, a major factor that caused the degradation in the long-term performance of the clock is the light shift from the unstable pump and probe lasers in the modulation transfer spectroscopy technique used in stabilizing the laser, the long-term temperature drift of the reference atoms, and the frequency drift of the locking point induced by the EOM crystal alongside residual amplitude modulation (RAM) noise. Precise control over the temperature and voltage of the EOM minimized the RAM [143]. As recommended by the authors, the frequency stability of the optical standard can be further improved by optimization of the parameters such as, the temperature of the vapor cell, the laser power stabilization, the bandwidth of the servo feedback loop, and by better vibration isolation of the system [143].

Table 3. Summarizes the cesium vapor cell two-photon optical scheme. The Cs microcell scheme by Gushing et al.[142] achieved a stability performance of 1.9×10^{-13} , which is comparable with the conventional vapor cell scheme. The best light shift value is by Fendel et al., with a value of -12.89Hz/mW [195]. Other parameters are shown, such as the signal linewidth, cell temperature, and longest reported fractional frequency instability.

Article	Signal Linewidth (MHz)	Beam waist (mm)	Cell Temperature(°C)	Light Shift (Hz/mW)	Pressure Shift (kHz/Pa)	longest reported Fractional Frequency Instability
Shi et al. 2024 [143]	0.03995	$N/R\ddagger$	35	30000	$N/R\ddagger$	3.3×10^{-12} at 10^4 s
Gusching et al. 2021 [142]	14.2	2	62	$N/R\ddagger$	$N/R\ddagger$	1.9×10^{-13} at 10^3 s
Wu et al. 2013 [187]	1.398	0.2	81	-76.92	$N/R\ddagger$	$N/R\ddagger$
Chen et al. 2011 [188]	1.2	$N/R\ddagger$	$N/R\ddagger$	$N/R\ddagger$	-290	3.0×10^{-13} @ 400 s
Cheng et al. 2007 [190]	$N/R\ddagger$	0.15	95	-179	-475	$4.4 \times 10^{-13**}$ @ 60 s
Fendel et al. 2007[195]	1.2	0.72	22	-12.89	$N/R\ddagger$	5.0×10^{-11}
Hagel et al. 1999 [191]	1.89	0.38	<110	-54	-90	4.4×10^{-13} @ 60 s

** Estimated value from spectroscopy
‡ Not reported

3.4. Microcell-Based Optical Frequency Standards

Wall-coated cells are good candidates for realizing high-performance or microfabricated devices, such as miniaturized atomic clocks /magnetometers [199]. Miniaturized vapor cells play a pivotal role in addressing the growing demand for compact, low-power, and robust atomic devices used across a wide range of applications, including atomic clocks, magnetometers, and quantum sensors. However, this reduction in size comes at the expense of short-term performance degradation [200]. The advancements in semiconductor and microelectromechanical systems (MEMS) have significantly driven the miniaturization of vapor cells, enabling wafer-scale manufacturing and mass production through microfabricated techniques [98,201]. Such innovations have paved the way for the next generation of compact atomic frequency standards, integrating optical components like lasers and spectroscopy units directly around the vapor cells [66,114].

Microcells are commonly fabricated via silicon wafer micromachining using anodic bonding techniques [100,144,148]. The fundamental fabrication process typically involves wafer-through etching of silicon, incorporation of an alkali metal source, and vacuum-tight sealing of the cells under appropriate buffer gas conditions [202]. Knappe et al. [201] further enhanced long-term frequency stability by presenting a novel cell-filling technique that substantially reduces the residue of chemicals inside the cell, thereby producing cells providing cleaner signals and that last long.

Chip-scale atomic clocks (CSAC) [98,201] exploit ground-state microwave reference transitions in alkali atoms confined within microfabricated vapor cells [148]. These devices have grown rapidly out of a convergence of atomic spectroscopy, silicon micromachining, and semiconductor laser technology, combining small size and low power [79]. The Coherent Population Trapping (CPT) method commonly employed in these cells enables extreme miniaturization and low power consumption; however, it suffers from limited signal contracts and increased sensitivity to light-shift effects [128,148], with a reported accuracy of about $1 \mu\text{s}$ per day [203].

Recent studies on microcell optical clocks specifically leveraged microfabricated vapor cells operating in the optical domain. Callejo et al. [114] characterized the short-term stability of a microcell optical frequency reference based on two-photon single-color excitation of the $^{87}\text{Rb } 5S_{1/2}(f=2) - 5D_{5/2}(F=4)$ transition at 778.1 nm. Despite efficient characterization, the presence of contaminants in their cell induced line broadening and compromised stability, with frequency locking being sensitive to line pulling and frequency hopping [114]. Moreover, no buffer gas was introduced before the cell sealing, but atmospheric helium permeation resulted in additional linewidth broadening, contributing ≈ 4 mTorr to the signal [79,114]. Furthermore, micro-optic breadboard approaches have also been demonstrated by Zachary et al. [110], showing a performance of $4.4 \times 10^{-12}/\sqrt{\tau}$ using two interlocked microcombs [110]. The direct use of optical frequency combs for spectroscopy and atomic clock development presents a promising alternative approach [62,115,166,204]. Such approaches leverage the inherent stability and broadband capabilities of frequency combs, potentially enabling even more compact and efficient frequency standards. We direct the reader to [142,148,205] for microcell standards based on other techniques, such as dual-frequency sub-Doppler spectroscopy [142], double-resonance Ramsey scheme [148], and CPT [205]

Ongoing developments in laser technology, coherent excitation techniques, and surface coating methods continue to drive improvements in microcell frequency standards [145]. Although coatings can enhance performance, uncoated cells are also utilized due to simplicity and cost-efficiency [79]. Optimizing microcell frequency standards could involve improving the fluorescence collection efficiency and employing more intense atomic transitions, such as those available from ^{85}Rb for atomic signal enhancement [114]. Additionally, the use of lasers with lower frequency noise could potentially improve the short-term frequency stability of microcells [110,114].

4. Short-Term-Performance Metrics and Limitations

The short-term frequency stability of vapor cell based optical references is predominantly limited by two noise processes: photon shot-noise (PSN) [121,206,207]—resulting from the limited number of fluorescence photons reaching the photodetector due to quantum statistical noise—and intermodulation noise—resulting from laser frequency fluctuations [98,114,118,208]. The short-term stability of an optical clock can be estimated using the following relation [118,121]

$$\sigma(\tau) = \frac{\Gamma}{\omega_{2ph}} \frac{1}{SNR} \quad (1)$$

Here, ω_{2ph} represents the transition frequency of the two-photon process, SNR is the signal-to-noise ratio of the measured atomic signal, and Γ is the transition linewidth of the signal [118,121]. Figure 5 summarizes the short-term stability of various standards at 1 s. The best performance is observed with the Rb vapor cell clock using the two-color scheme, demonstrating a stability of 1.5×10^{-13} by Perrella et al. [122].

4.1. Photon Shot-Noise

Photon shot-noise (PSN) arises fundamentally due to the quantum nature of light and the inherent randomness (spontaneous emission) of photon arrival at detectors [121,122,209]. It sets a fundamental limit to the signal-to-noise ratio (SNR) of an optical detection system, described by [209]

$$SNR_{photon} = 10 \log_{10} \mu \quad (2)$$

where μ is the mean photon number detected over a specific time interval. This noise is independent of the detector electronics and can be reduced only by increasing the light intensity or extending the exposure time [209]. The impact of PSN on two-photon processes is particularly significant due to their inherently low absorption efficiency [114,160] and the limitation of the collection efficiency of

detectors on the photocurrent of the detector [122]. For a frequency standard limited by shot-noise, the stability will improve by $1/\sqrt{\tau}$ for a longer averaging time as given by [121]

$$\sigma(\tau) \propto \frac{\Gamma}{\omega_{2ph}} \frac{1}{SNR} \cdot \frac{1}{\sqrt{\tau}} \quad (3)$$

τ is the averaging time. Improved SNR through higher laser power or elevated cell temperature could partially mitigate this limitation [114]. However, these variations in the quantum efficiency of detectors and different beam sizes might influence the measured values of the light shift [187]. These factors, though significant, do not affect the determination of the intrinsic frequency of the atomic transition, which is extrapolated from conditions where external light fields are absent [187].

4.2. Intermodulation Effect

The Intermodulation effect is prominent in free-running continuous-wave optical frequency references due to laser frequency fluctuations that convert into intensity noise via the atomic absorption profile [114,119,142,208]. The short-term stability degradation due to intermodulation can be quantified as [114,159]

$$\sigma_y(\tau) = \frac{1}{2} \sqrt{\frac{S_v(2f_m)}{v_0^2}} \cdot \frac{1}{\sqrt{\tau}}$$

$S_v(2f_m)$ is the frequency noise power spectral density evaluated at twice the modulation frequency f_m , and v_0 is the optical carrier frequency. Various studies confirm intermodulation noise as a critical factor limiting the short-term stability of miniaturized optical frequency standards [109,110,142]. This effect can be minimized by using lasers with relatively low noise [119].

4.2.1. Background Noise

Background noise, particularly ambient infrared radiation, can also be a source of noise in the detector performance. Most detectors are manufactured such that noise from other sources is negligible, approaching performance limited only by photon shot-noise. Hence, a good detector should have high quantum efficiency, low dark current, high sensitivity, and excellent linearity [209]. Practical methods such as high dichroic optics, long-pass filtering, and eternal shielding (e.g., black boxes) are effective strategies for minimizing laboratory ambient noise interference [185,210] and scattered light from the clock excitation laser for increased SNR [210]. Additionally, any electronics in the clock system, such as cables, lock-in amplifiers, and noise in the feedback loop, all contribute to the short-term stability of the clock.

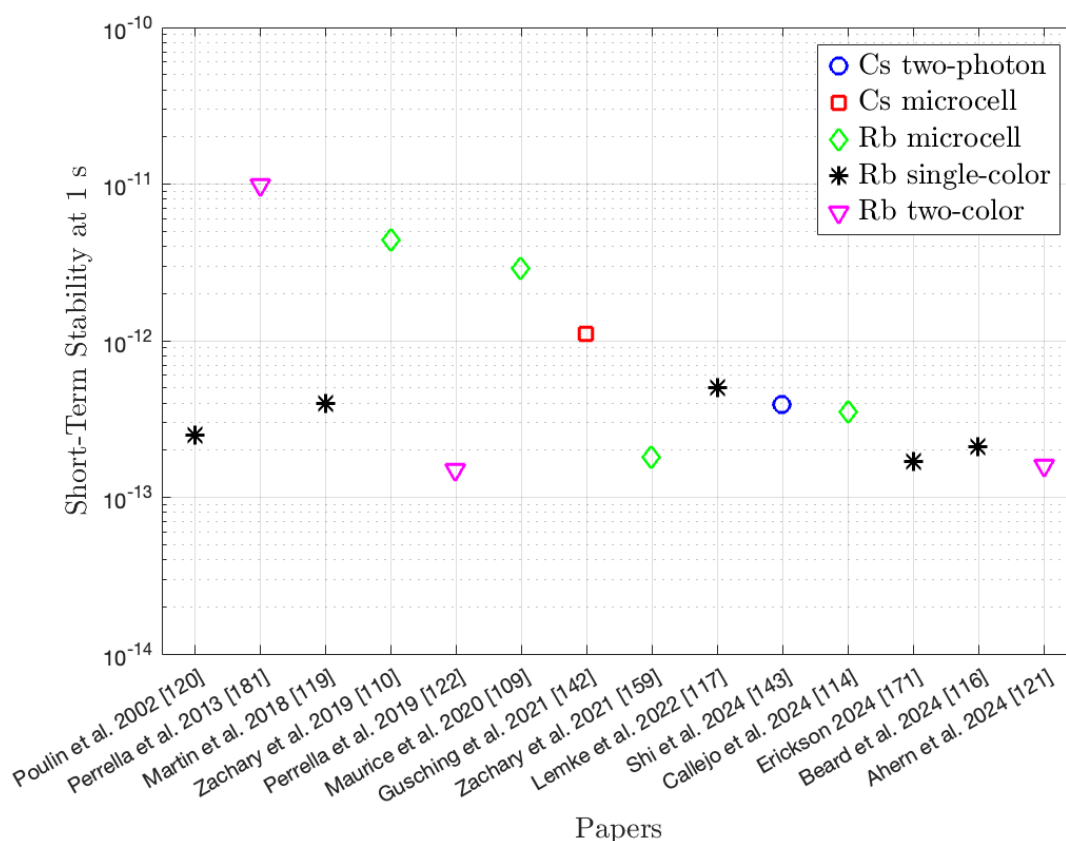


Figure 5. Shows the summary of the reported short-term stability of various standards at 1 s. From this graph, the best short-term stability is the two-color scheme by Perrella et al. [122], which achieved a stability of 1.5×10^{-13} .

5. Long-Term Performance Limiting Effects

Several factors can degrade the long-term performance of optical atomic clocks. However, the light shift is the most dominant and persistent source of frequency instability, particularly in the long-term accuracy and reliability of vapor cell optical clocks. Hence, there is a need for focused attention on understanding and controlling light shifts. This section provides an in-depth discussion of the light shift effect.

5.1. Light Shift Theory and Discussion

Atoms interact with external fields, such as those from a laser field, which, when tuned to resonance with the atom's transition frequency, simultaneously excites the atom from a lower to a higher energy state and also induces shifts in the atomic energy levels relative to the laser frequency. This phenomenon, known as the AC Stark shift or light shift, is a second-order perturbative effect that fundamentally alters atomic energy levels during light field interactions [211,212]. Initially detailed by Cohen-Tannoudji in 1962 [213], the light shift has since been recognized as a principal limiting factor for the long-term stability and performance of atomic clocks.

As stated by Levi et al. [214], the AC Stark shift inherently involves at least a two-photon process, complicated further by the non-intuitive influence of stochastic fields on multi-photon processes [214]. This shift is influenced by multiple factors including the frequency and intensity of the light [127,160,177,178,207], as well as the laser frequency detuning from the intermediate $5P_{3/2}$ energy level [160,215] exhibiting a dual nature depending on field strength — quadratic shifts occur in weak fields, and linear shifts in strong fields [171,216].

Additionally, fluctuations in laser power, changes in the transmittance of the optical cell window (aging of cells), cell temperature fluctuations [217], and imperfect or unstable optical alignment of the interrogation beams can also contribute to Stark shift fluctuations and clock instabilities [109,172]. It is important not to ignore dephasing processes in the full optical frequency dependence of the AC Stark shift near resonance, where photon scattering is most substantial [214]. This phenomenon significantly impacts optical clock performance, contributing to output drifts and noise that limit long-term stability [127,140,148,159]. Unfortunately, the light shift cannot be completely eliminated in two-photon spectroscopy because the transition between levels is made by virtual, dipole-allowed transitions through intermediate states that are usually far from resonance [218,219].

To mitigate light shift, it is helpful to have a comprehensive understanding of the theory behind it. We start from the simplest case of a two-level system coupled by an electric dipole transition of frequency ω_{eg} (as discussed in [220]).

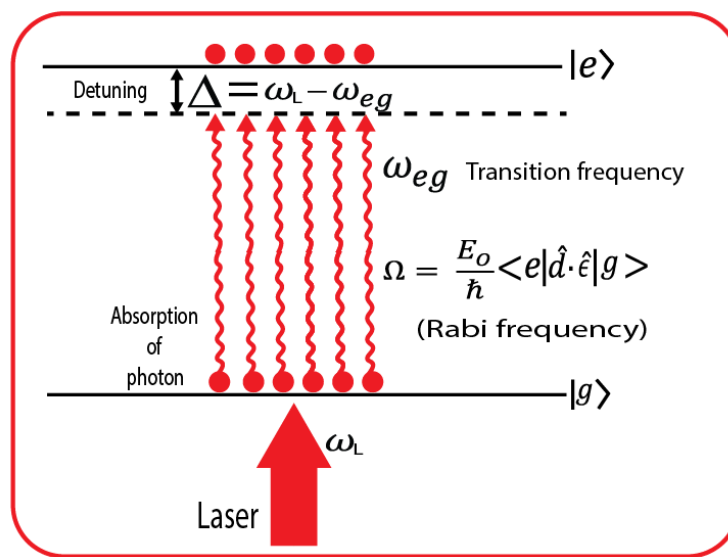


Figure 6. Typical two-level energy system in a vapor cell with multiple atoms participating in light-atom interaction coupling. Upon absorbing a photon, the atoms move from the ground state $|g\rangle$ to the excited state $|e\rangle$. The Rabi frequency depicts the coupling strength between the atoms and the applied field, and ω_{eg} is the frequency at which the atoms transition to the excited state.

Assuming the field is near resonance between the ground state $|g\rangle$ and an excited state $|e\rangle$, the laser frequency $\omega_L \approx \omega_{eg} \equiv \frac{E_e - E_g}{\hbar} \equiv \frac{E_b - E_a}{\hbar}$; where E_g and E_e represent the energy of the ground and excited states respectively, and \hbar is the reduced Planck's constant. The detuning, which is the difference from the resonance of the laser's frequency relative to the atom's resonant frequency $\Delta = \omega_L - \omega_0$ can be examined from the time-dependent Schrödinger equation, which governs the system's evolution. It is given by the following [220]

$$i\hbar \frac{\partial \Psi(\mathbf{r}, t)}{\partial t} = \hat{H} \Psi(\mathbf{r}, t) \quad (4)$$

where Ψ represents the wavefunction, \hat{H} the Hamiltonian operator, given by $\hat{H} = \hat{H}_0 + \hat{H}_{int}$, with \hat{H}_0 being the Hamiltonian of the unperturbed atom with eigenstates $|g\rangle$ and $|e\rangle$, and $\hat{H}_{int} = -\mathbf{d} \cdot \mathbf{E}$, is the time-dependent perturbation or interaction Hamiltonian operator. The dot product indicates the projection of the dipole along the direction of the electric field. The total atomic wave function at any given time t can be written as a superposition of the ground and excited state. That is,

$$i\hbar \frac{\partial}{\partial t} [c_g(t)|g\rangle + c_e(t)|e\rangle e^{-i\omega_{eg}t}] = \hat{H}_0 + \hat{H}_{int} [(c_g(t)|g\rangle + c_e(t)|e\rangle e^{-i\omega_{eg}t})]$$

c_g and c_e are the coefficients of the ground and excited states, respectively, and ω_{eg} is the frequency between the ground and excited state.

The electric field of a plane wave can be written as $\mathbf{E} = \hat{\mathbf{e}}E_0 \cos(kr - \omega t)$, where $\hat{\mathbf{e}}$ is the polarization vector, E_0 is the amplitude of the field, k and r are the wave and position vectors respectively, and t represents the interaction time. Assuming the atom is much smaller than the wavelength of the light (dipole approximation), the spatial variation of the electric field across the atom can be neglected ($k \cdot r \approx 0$). i.e., the value of r is small compared to the wavelength λ . We can express the electric field as $\mathbf{E} = \hat{\mathbf{e}}E_0 \cos(\omega t)$. Let $\omega = \omega_L$. Hence,

$$i\hbar \frac{dc_g(t)}{dt} = c_e \langle g | \hat{\mathbf{d}} \cdot \hat{\mathbf{e}} E_0 \cos(\omega_L t) | e \rangle e^{-i\omega_{eg}t} \quad (5)$$

$$i\hbar \frac{dc_e(t)}{dt} = c_g \langle e | \hat{\mathbf{d}} \cdot \hat{\mathbf{e}} E_0 \cos(\omega_L t) | g \rangle e^{i\omega_{eg}t} \quad (6)$$

$$i\hbar \frac{dc_g(t)}{dt} = c_e \hbar \frac{E_0}{\hbar} \cos(\omega_L t) \langle g | \hat{\mathbf{d}} \cdot \hat{\mathbf{e}} | e \rangle e^{-i\omega_{eg}t} \quad (7)$$

$$i\hbar \frac{dc_e(t)}{dt} = c_g \hbar \frac{E_0}{\hbar} \cos(\omega_L t) \langle e | \hat{\mathbf{d}} \cdot \hat{\mathbf{e}} | g \rangle e^{i\omega_{eg}t}. \quad (8)$$

In terms of Euler's formula, we have

$$i\hbar \frac{dc_g(t)}{dt} = c_e \hbar \left(\frac{e^{i\omega_L t} + e^{-i\omega_L t}}{2} \right) e^{-i\omega_{eg}t} \times \frac{E_0}{\hbar} \langle g | \hat{\mathbf{d}} \cdot \hat{\mathbf{e}} | e \rangle \quad (9)$$

$$i\hbar \frac{dc_e(t)}{dt} = c_g \hbar \left(\frac{e^{i\omega_L t} + e^{-i\omega_L t}}{2} \right) e^{i\omega_{eg}t} \times \frac{E_0}{\hbar} \langle e | \hat{\mathbf{d}} \cdot \hat{\mathbf{e}} | g \rangle. \quad (10)$$

We can define a new variable Ω , known as the Rabi frequency, where

$$\Omega = \frac{E_0}{\hbar} \langle e | \hat{\mathbf{d}} \cdot \hat{\mathbf{e}} | g \rangle. \quad (11)$$

The Rabi frequency characterizes how strongly an atomic transition is driven by an external electric field. Its magnitude scales with the field's intensity, and, at a fixed intensity, it is determined by the atomic states involved and the polarization of the field, as expressed through the dipole matrix element [220].

By distributing the exponential term $e^{-i\omega_{eg}t}$, the coupled equations (7) and (8) can now be written as,

$$i\hbar \frac{dc_g(t)}{dt} = c_e \frac{\hbar \Omega^*}{2} \left(e^{i(\omega_L - \omega_{eg})t} + e^{-i(\omega_L + \omega_{eg})t} \right) \quad (12)$$

$$i\hbar \frac{dc_e(t)}{dt} = c_g \frac{\hbar \Omega}{2} \left(e^{i(\omega_L + \omega_{eg})t} + e^{-i(\omega_L - \omega_{eg})t} \right) \quad (13)$$

where $\omega_L - \omega_{eg}$ refers to the detuning (i.e., the difference frequency between the light field and the resonant two-level frequency) and ω_{eg} will be represented as Δ . The rotating wave approximation (RWA) can be applied for light-field interaction at near-resonance. In addition, slowly varying amplitudes, $\omega_L + \omega_{eg}$, oscillate fast, which averages out and can, therefore, be neglected. The uncoupled equation, which oscillates at the Rabi frequency, is given as,

$$\frac{d^2 c_g}{dt^2} - i\Delta \frac{dc_g}{dt} + \frac{\Omega^2}{4} c_g = 0 \quad (14)$$

$$\frac{d^2 c_e}{dt^2} + i\Delta \frac{dc_e}{dt} + \frac{\Omega^2}{4} c_e = 0. \quad (15)$$

For a simplest case of zero detuning (i.e $\Delta = 0$ ($\omega_L = \omega_{eg}$)), the equation simplifies further. However, if we assume that at $t = 0$, $c_g = 1$ and $c_e = 0$, then the above-uncoupled equations can be solved to give the expression for the probability to be in the excited state $|c_e(t)|^2$ [220]. By explicitly writing out Ω' typically an exponential solution for c_e is assumed giving,

$$|c_e(t)|^2 = \frac{\Omega^2}{\Omega^2 + \Delta^2} \sin^2\left(\frac{\sqrt{\Omega^2 + \Delta^2} \cdot t}{2}\right). \quad (16)$$

showing the dependence on the Rabi frequency Ω and the detuning Δ . Since there are two frequencies in the system (that of the atom and laser), with the frequency of the laser close to that of the atom, the rotating frame of the laser can be similarly considered with new coefficients c'_g and c'_e

$$\Psi(\mathbf{r}, t) = c'_g(t)|g\rangle + c'_e(t)|e\rangle e^{-i\omega_{eg}t}. \quad (17)$$

Following the same argument for the laser's rotating frame. We can reformulate them to remove the explicit time dependence on the right-hand side by defining new coefficients $c'_g = c_g$ and $c'_e = c_e e^{-i\Delta t}$. Therefore,

$$i\hbar \frac{d}{dt} c'_e = -\hbar \Delta c'_e + c'_g \frac{\hbar \Omega}{2} \quad (18)$$

and the Hamiltonian can be written in Matrix form and diagonalized as

$$\begin{vmatrix} -\lambda & \frac{\hbar \Omega}{2} \\ \frac{\hbar \Omega}{2} & -\hbar \Delta - \lambda \end{vmatrix} = 0 \quad (19)$$

This can be solved to obtain

$$\lambda = \frac{\hbar}{2} \left(-\Delta \pm \sqrt{\Omega^2 + \Delta^2} \right) \quad (20)$$

$$E_g = \frac{\hbar}{2} \left(-\Delta + \sqrt{\Omega^2 + \Delta^2} \right) \quad (21)$$

$$E_e = \frac{\hbar}{2} \left(-\Delta - \sqrt{\Omega^2 + \Delta^2} \right) \quad (22)$$

Far from resonance under the weak coupling condition where the Rabi frequency is much less than the transition frequency ($\Omega \ll |\Delta|$) we can Taylor expand the square root around $\frac{\Omega}{\Delta} \rightarrow 0$

$$\sqrt{\Omega^2 + \Delta^2} = \Delta \sqrt{1 + \left(\frac{\Omega}{\Delta}\right)^2} \approx \Delta + \frac{\Omega^2}{2\Delta} \quad (23)$$

Substituting into the eigenvalue equations, we get

$$E_g \approx \frac{\hbar \Omega^2}{4\Delta} \quad (24)$$

$$E_e \approx -\hbar \Delta - \frac{\hbar \Omega^2}{4\Delta} \quad (25)$$

The overall sign depends on the sign of the detuning. Intuitively, we can say that far from resonance, the excited state E_e is shifted downwards by $\frac{\hbar \Omega^2}{4\Delta}$, and the ground state E_g is shifted upwards by the same amount. Hence,

$$\Delta E = \frac{\hbar \Omega^2}{4\Delta} \quad (26)$$

By substituting the Rabi frequency from equation (11),

$$\Delta E = \frac{E_0^2}{4\hbar\Delta} \langle e | \hat{d} \cdot \hat{\epsilon} | g \rangle^2 \quad (27)$$

The expression for the shift (ΔE) is proportional to the square of the electric field amplitude, which is proportional to the light intensity. As seen below,

$$I = \frac{1}{2} \epsilon_0 c E_0^2 \text{ (W/m}^2\text{)}$$

$$E_0 = \sqrt{\frac{2I}{c\epsilon_0}} \text{ (V/m)} \quad (28)$$

Therefore, light shift

$$\Delta E = \frac{I}{2\hbar\Delta c\epsilon_0} \langle e | \hat{d} \cdot \hat{\epsilon} | g \rangle^2 \quad (29)$$

By implementing equation (29) for the $5S_{1/2} - 5P_{1/2}$ transition in Rb-87, we plot the light shift as a function of detuning for various intensities as shown in Figure 7. Where \hbar is the reduced Planck constant, Δ is the D1 detuning between the two-state, c is the speed of light, ϵ_0 is the permittivity of free space, and $\langle e | \hat{d} \cdot \hat{\epsilon} | g \rangle$ is the transition dipole matrix element of the transition $5S_{1/2} - 5P_{1/2}$. The value for the transition matrix element was taken from Steck's article on Rb 87 D line data [221].

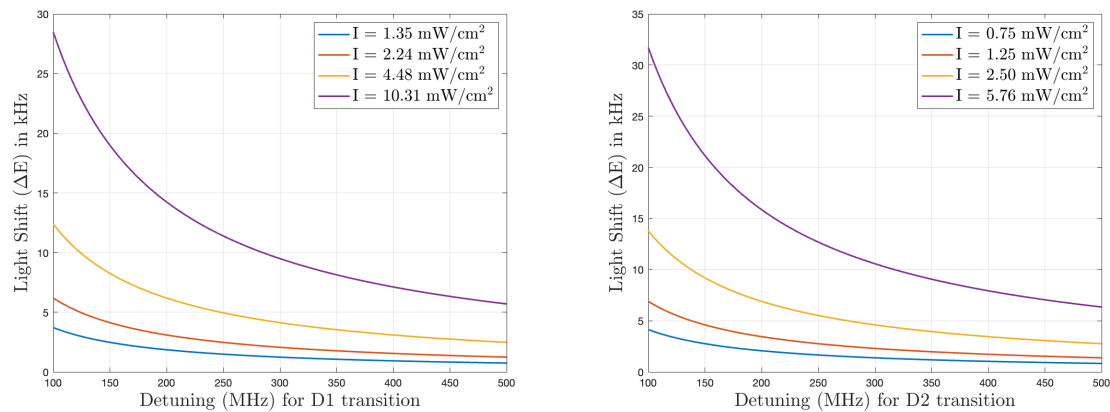


Figure 7. Plotted from equation (29), shows a visualization of light shift as a function of detuning (Δ), and different intensities for a two-level Rb 87 D1 transition ($5S_{1/2}$ to $5P_{1/2}$) as shown on the left plot, and D2 transition ($5S_{1/2}$ to $5P_{3/2}$) as shown on the right. The light shift decreases for larger detunings, which aligns with the inverse proportionality, and it increases for higher laser intensities.

5.1.1. Beyond Two-Level System

In a system with more than two energy levels, estimating the AC Stark shift becomes complex. This involves multiple energy levels in an atom and their interactions with the oscillating electric field of the laser. Hence, careful consideration must be made of the perturbation of each atomic state due to the off-resonant coupling with the laser field. As discussed in reference [177,222], to successfully estimate the AC Stark shift, accurate values of the electric dipole matrix element and parameterization of the scalar and tensor dynamic polarizability, which determines the strength of the light shift associated with the relevant clock transition, are needed [177]. For the scalar light shift consisting of the sum of off-resonant virtual transitions linked to various optical transitions, the laser polarization and the Zeeman structure of the coupled states play no significant role [214]. In contrast, the tensor light shift is influenced by the quadrupole symmetry characteristics of different hyperfine transitions, which vanish if the structure of the excited-state hyperfine structure remains unresolved

[214]. Stark shifts are obtained as the energy eigenvalues of the Schrodinger equation with interaction operator H_{int} , representing the effect of the external field on the atomic system.

$$\hat{H} = \hat{H}_{atom} + \hat{H}_{int} \quad (30)$$

$$\hat{H}_{int} = -\vec{E} \cdot \vec{d}, \quad (31)$$

where \vec{E} is the applied external electric field and \vec{d} is the electric-dipole operator.

The selection rules for electric dipole transitions dictate that the parity must change for a state to have a non-zero electric dipole moment or a dipole-allowed transition, so it is only the superposition of states of different parity that will contribute [168,223]. The first-order shift associated with the interaction operator H_{int} vanishes in alkali-metal atoms (due to their spherical symmetry). If the dipole matrix element vanishes, the transition may still occur through higher-order processes [220]. Moving to the second-order term of the perturbation expansion, the lowest-order correction to the energy of the atom in $|n\rangle$ is given by

$$\Delta E_n^{(2)} = \sum_{n \neq k} \frac{|\langle n | \mathbf{d} \cdot \mathbf{E} | k \rangle|^2}{E_n - E_k} = \sum_k \frac{|\langle n | \mathbf{H}_{int} | k \rangle|^2}{E_n - E_k} \quad (32)$$

$$\Delta E_n^{(2)} = \sum_k \frac{\langle n | H_{int} | k \rangle \langle k | H_{int} | n \rangle}{E_n - E_k}, \quad (33)$$

$\Delta E_k^{(2)}$ represents the second-order energy shift for the state n . n and k are unperturbed atomic states with energies E_n and E_k , respectively. The sum over k includes all the permissible intermediate states by electric-dipole transition selection rules while $|\langle n | \mathbf{H}_{int} | k \rangle|^2$ is the squared magnitude of the matrix element of the dipole interaction between state n and state m in the presence of an external electric field \mathbf{E} .

Using the Wigner-Eckart theorem, which re-expresses matrix elements in terms of how they transform under the system's symmetries, written as,

$$\langle j_f m_f | T_q^{(k)} | j_i m_i \rangle = \frac{\langle j_i m_i k q | j_f m_f \rangle}{\sqrt{2j_f + 1}} \langle j_f || T^{(k)} || j_i \rangle \quad (34)$$

where $\langle j_f m_f | T_q^{(k)} | j_i m_i \rangle$ is the matrix element of a spherical tensor operator $T_q^{(k)}$ of rank k and components q , between the initial and final states with total angular momenta j_i and j_f , and their z -components m_i and m_f , respectively. $\langle j_i m_i k q | j_f m_f \rangle$ represents the Clebsch-Gordan coefficient for adding two angular momentum states, while $\langle j_f || T^{(k)} || j_i \rangle$ is the reduced matrix element, which is independent of the magnetic quantum numbers. The factor of $\frac{1}{\sqrt{2j_f + 1}}$ is a redefinition of the reduced matrix elements [224]. Therefore,

$$\Delta E_n^{(2)} = \sum_k \frac{\langle n | H_{int} | k \rangle \langle k | H_{int} | n \rangle}{E_n - E_k} \quad (35)$$

The energy shift of state n , due to a time-varying electric field with frequency ω , is proportional to the dynamic polarizability of the state $\alpha(\omega)$. Thus, the light shift of a transition, ΔE , is the difference between the perturbation in energy experienced by the two levels in the transition

$$\Delta E = -\frac{1}{2} |E|^2 \Delta \alpha(\omega), \quad (36)$$

Hence, we can re-write ΔE by expressing the atomic differential polarizability $\alpha(\omega)$ between the ground, g , and excited, e , states of the affected transition, [177]

$$\Delta\alpha(\omega) = \alpha_g(\omega) - \alpha_e(\omega). \quad (37)$$

The dynamic polarizability of the state n may be expressed in terms of scalar (trace), vector (free symmetric), and tensor (anti-symmetric) components $\alpha_0(\omega)$, and $\alpha_2(\omega)$ [141,156,225]. However, the vector tensor becomes important for circularly polarized light, as the two-photon transition is pumped with linearly polarized light, resulting in a zero vector shift [156].

$$\alpha(\omega) = \alpha_0(\omega) + \alpha_2(\omega) \left(\frac{3m_n^2 - J_n(J_n + 1)}{J_n(2J_n - 1)} \right), \quad (38)$$

where J_n and k_n are the total angular momentum and its projection [177]. The scalar polarizability, which results in an AC Stark shift [156], is given by,

$$\alpha_0(\omega) = \frac{2}{3(2J_n + 1)} \sum_k \frac{\omega_{kn} |\langle n || d || k \rangle|^2}{\omega_{kn}^2 - \omega^2}, \quad (39)$$

where $|\langle n || d || k \rangle|^2$ are reduced electric dipole (E1) matrix elements and ω_{kn} are transition frequencies. Similarly, the tensor polarizability is expressed in terms of the reduced E1 matrix elements [226] in the following way:

$$\alpha_2(\omega) = C \sum_n (-1)^{J_n + J_k} \begin{Bmatrix} J_n & 1 & J_k \\ 1 & J_k & 2 \end{Bmatrix} \frac{\omega_{kn} |\langle n || d || k \rangle|^2}{\omega_{kn}^2 - \omega^2}, \quad (40)$$

with the normalization coefficient,

$$C = 4 \left(\frac{5J_n(2J_n - 1)}{6(J_n + 1)(2J_n + 1)(2J_n + 3)} \right)^{1/2}, \quad (41)$$

The light shift in equation (36) becomes

$$\Delta E = -\frac{1}{2} \alpha_0(\omega) E^2 - \frac{1}{2} \alpha_2(\omega) \frac{3m_j^2 - j_n(j_n + 1)}{j_n(2j_n - 1)} E^2, \quad (42)$$

The polarizabilities are calculated using all-orders relativistic many-body methods described in [177, 226,227].

The laser frequency ω is assumed to be several linewidths off-resonance. Here, the polarization vector of the light defines the z-direction [222]. From equations (39) and (40), we observe that a full spectrum of intermediate states is required to calculate the polarizabilities. By applying the energy values and the values of the reduced matrix elements listed in reference [172], we evaluate different values of the atomic polarizability for $n' = 5, 6, 7$ and 8 [228] of Rb-87 in,

$$\alpha_v^{ns}(\omega) = \frac{1}{3} \sum_{n'} \left(\frac{(E_{n'p_{1/2}} - E_{ns}) |\langle n' p_{1/2} || \mathbf{D} || ns \rangle|^2}{(E_{n'p_{1/2}} - E_{ns})^2 - \omega^2} + \frac{(E_{n'p_{3/2}} - E_{ns}) |\langle n' p_{3/2} || \mathbf{D} || ns \rangle|^2}{(E_{n'p_{3/2}} - E_{ns})^2 - \omega^2} \right), \quad (43)$$

with the plot of the rubidium D1 ($5S_{1/2} - 5P_{1/2}$) and D2 ($5S_{1/2} - 5P_{3/2}$) resonance lines of the polarizability against wavelength in Figure 8. The zero crossing point produces no light shift because the differential AC Stark shift between the ground and excited state cancels out. One way to suppress light shift is to tune the pumping light to this zero crossing frequency (magic wavelength), which depends

on the temperature and composition when used in optical pumping [125,229]. However, this does not completely solve the problem of light shift because the magic wavelength is only for some specific transitions, and the D1 and D2 transitions and other intermediate states are in the rubidium transition, which is typically a multi-level system accounting for all higher-order contributions, as seen from Figure 8. A similar plot is shown in [141,228].

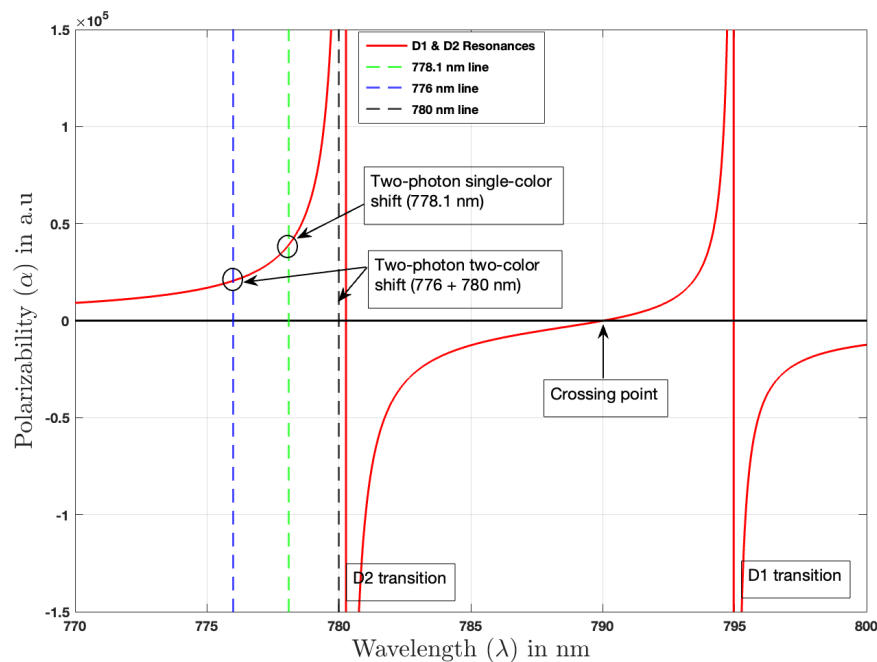


Figure 8. Shows the D1 ($5S_{1/2} - 5P_{1/2}$) and D2 ($5S_{1/2} - 5P_{3/2}$) plot of the dynamic polarizability for the ground state of rubidium 87. The little circles show the non-zero contributions of the polarizability on both the single-color (778.1 nm) and two-color (776 nm + 780 nm) wavelengths, which is directly proportional to the light shift. Evidently, light shift cannot be eliminated in a single-color transition but can be minimized, while the two-color transition has the advantage of reduced light shift, in addition to the flexibility of tuning both lasers, such that the light shift produced by one cancels the other.

As clearly explained by Perrella [160], a two-color and single-color excitation will yield approximately the same sensitivity to incident power fluctuation in situations where the two-color excitation beams have about the same power [160]. Therefore, if the power of the two-color beam could be adjusted separately and the detunings gradually tuned from the intermediate state, the magnitude of the light shift effect can be minimized [160].

5.2. Vapor Cell Temperature Fluctuation and Drift

Temperature fluctuations within vapor cells significantly degrade the long-term performance of vapor cell optical clocks. Atomic collisions within the vapor cell can alter the wave function of the ground and excited states, leading to frequency shifts directly correlated to changes in atomic density [143]. Shi et al. [143] highlight that even a minor temperature fluctuation of $0.1\text{ }^{\circ}\text{C}$ can cause a density change on the order of 10^{11} cm^{-3} . They emphasize that the vapor cell's temperature stability largely depends on the cold finger, with temperature directly influencing the atomic density and thus inducing frequency drift. Furthermore, such temperature instabilities result in collisional frequency shifts and fluctuations in the signal-to-noise ratio of the modulation transfer spectroscopy and negatively impact the fractional stability of the frequency standards [143].

To mitigate this effect, active monitoring and precise temperature control of the vapor cell’s cold spot is essential to reduce most frequency shift and line-broadening issues [218]. Typically, optical references employing two-photon transitions operate around 100 °C [119]. However, Maurice et al.[109] operated their miniaturized rubidium optical clock at a cell temperature of 80 °C to reduce long-term drift without compromising short-term stability or locking robustness. Using a lower temperature had a drawback of decreasing the number of interacting atoms participating in signal strength. Nguyen and Schibli [136] proposed a two-photon, two-color scheme for suppressing temperature-induced shifts in a warm Rb vapor clock without trading off the AC Stark shift for an increased sensitivity to the cell temperature or pressure. Their approach utilized the flexibility of the two-color method to cancel the residual Doppler shift against frequency shifts caused by cell temperature variations without requiring specialized buffer gases [136]. An additional practical mitigation strategy test in cesium vapor standards was proposed by Shi et al. [143], which involves incorporating an insulating functional layer to significantly reduce the impact of temperature fluctuations [143]. Therefore, precise temperature stabilization to mitigate temperature-induced frequency shifts remains a critical area of research for achievable long-term performance.

6. Other Performance Limiting Effects

Various other perturbing factors can contribute to limiting the medium-to-long-term performance of a clock if neglected and not carefully characterized during measurements. Below, we briefly discuss and present a table (Table 4) summarizing the key factors as reported by some authors. Thereafter, we discuss some important observations that contribute to the stability of standards.

Table 4. Two experimentally comparable schemes with limiting effects that restrict the overall performance of vapor cell optical clock is summarized. As observed from the table, both authors reported the same values of quadratic Zeeman shift and the 2nd order Doppler induced shift and BBR shift but with opposite signs at ≈ 373 K. According to Martin et al., the BBR shift requires that the blackbody source be held to stable temperatures below 770 mK [119]. In addition, Martin et al. also characterize the frequency of their standard as a function of the vapor-cell temperature to be $-1.09 \pm 0.04 \times 10^{-12} \text{ K}^{-1}$, while Zachary et al. [110] did not report that shift. The scheme of Zachary et al. [110] also achieved a lower Helium collisional shift of 0.55×10^{-8} compared to the other. However, the overall experimental scheme of Martin et al. [119] achieved a lower fractional frequency instability and light shift value as previously presented in Table 1.

Author	Temperature Shift (K^{-1})	Helium Collision Shift (Torr^{-1})	2nd Order Doppler Shift (K^{-1})	Quadratic Zeeman Shift (G^{-2})	Blackbody Radiation (K^{-1})
Martin et al. 2018 [119]	$-1.09 \pm 0.04 \times 10^{-12}$	2.7×10^{-8}	1.0×10^{-15}	6.5×10^{-11}	1.3×10^{-15}
Zachary et al. 2019 [110]	$N/R \ddagger$	5.5×10^{-9}	-1.0×10^{-15}	6.5×10^{-11}	-1.3×10^{-15}

‡Not reported

6.1. The Stochastic Nature of the Laser-Field

Laser fields inherently exhibit stochastic fluctuations due to their quantum mechanical nature, and, are affected by flicker noise at low frequencies [230]. These fluctuations manifest primarily as random variations in both amplitude and phase, resulting in non-monochromatic laser output. Fundamentally, quantum noise, particularly phase noise arising from spontaneous emission, is unavoidable and limits the coherence of laser fields [207]. When dealing with weak fields under first-order perturbation theory, spectroscopy typically addresses this non-monochromatic nature by convolving the absorption cross-section with the laser’s power spectrum, which is valid for single-photon processes [231]. However, this convolution approach is insufficient for accurately describing the field’s stochastic nature in the two-photon transitions, requiring the AC Stark shift to be addressed for performance evaluation in the order of 10^{-16} . An important consequence of laser phase noise is its efficient conversion to

amplitude noise (PM-to-AM conversion) when a laser propagates through a resonant atomic vapor [150,232]. This phenomenon arises because the atomic coherence created by the laser field is sensitive to fluctuations in the laser's phase. Consequently, if the laser phase fluctuates, so does the phase of the atomic superposition state, affecting the absorption cross-section and thereby introducing intensity fluctuations into the transmitted laser beam [232]. Such a conversion can significantly amplify the relative intensity noise (RIN) of the transmitted laser. In some cases, by one to two orders of magnitude beyond the laser's intrinsic RIN [232].

These stochastic effects are particularly critical in vapor-cell atomic clocks, where the frequency noise of a diode laser couples directly to the clock instability through the light-shift effect [233]. The resulting optical frequency noise, transferred to atomic standards via the light shift effect, inherently limits the achievable stability of frequency standards [207,232]. Hence, the laser phase noise plays an essential role in directly contributing to the system's short-term instability and degradation of long-term stability due to its potential to broaden the atomic linewidth [231].

Mitigating these stochastic noise processes is essential for improving atomic clock performance. Techniques such as employing external-cavity diode lasers (ECDL) to reduce frequency modulation noise, using narrow linewidth lasers, implementing collision broadening to reduce atom sensitivity to laser fields, or operating under conditions where atoms become insensitive to rapid laser phase fluctuations can significantly enhance the stability of vapor-cell standards [98,110,231]. As reported by Zachary et al. [110], after calculating the phase noise of their clock from the laser frequency noise spectrum for low frequencies (<300 Hz), the phase noise is limited by the intrinsic phase noise of the clock laser [110]. Ultimately, understanding and controlling the stochastic nature of laser fields remains central to advancements in high-precision atomic spectroscopy and frequency standards.

6.2. Vapor Cell Design and Functionality

The vapor reference cells are at the heart of vapor cell-based atomic clocks, providing the vapor medium of specific atoms, such as rubidium or cesium. These cells, typically made from a conventional glassblowing technique, are baked and evacuated [79,200] to $<10^{-8}$ Torr to remove contaminants before filling with alkali atoms (Cs or Rb). The vapor cells are designed to be transparent to specific wavelengths corresponding to the optical transitions of the enclosed atoms [144], such as alkali atoms. In microwave atomic clocks, these cells often incorporate buffer gases like Argon or Neon to slow atom diffusion and reduce wall collisions to enhance the coherence lifetime of the atomic spins. Also, they may be coated with anti-relaxation materials like paraffin to prevent depolarization upon contact with the cell walls [145,146,199,234,235]. Such coatings allow atoms to bounce off the walls without losing their spin polarization, significantly reducing atomic coherence relaxation due to atom-wall and buffer gas collisions [79,145,152,236,237]. With paraffin wall-coated ^{87}Rb cell (14mm \times 14mm), short-term stability of $1.3 \times 10^{-12} / \sqrt{\tau}$ was demonstrated by Bandi et al. using the double resonance technique [237]. Similarly, Knappe and Robinson (2010) [235] have studied cells coated with anti-relaxation coating, along with buffer gas between 0 to 25 kPa in the ^{87}Rb vapor cell using microwave double resonance technique [235]. This is another alternate solution, which, in addition to other findings, revealed that the Nitrogen buffer gas did not significantly alter the wall coating [235]. Furthermore, a slight improvement in linewidth was found for cells with wall coating. However, the improvement decreases quickly with increased buffer-gas pressure [235]. The presence of buffer gas in microwave systems can reduce the resonance linewidth to < 40 Hz in systems like coherent population trapping (CPT), though it also may shift and broaden the resonance, affecting the CPT by mixing Zeeman sublevels [79,145,235] or pressure-broadening the excited states of alkali atoms [235].

John Kitching, in a review article, noted that an optimum buffer gas pressure exists for each cell diameter, balancing relaxation from wall collisions with that from buffer gas collisions [79]. He also observed that for a wall-coated cell, the linewidth decreases inversely with the cell diameter [79]. Wu et al. suggested sophisticated linewidth measurements as a guideline for choosing suitable cells for

better frequency accuracy [187]. In cesium vapor cells, a technique for preparing wall-coated cells with paraffin has also been demonstrated [238]

In contrast, optical clocks typically do not use buffer gas in the vapor cell. Helium permeation from ambient air into glass cells is a known issue that can cause collisional shifts and line broadening primarily due to dispersion in adsorption time [79,135,153,162,239], with helium contamination having a small contribution effect on the long-term stability of a clock [117,119]. Techniques like paraffin coatings, which feature lower adsorption energy than bare glass surfaces, mitigate these effects by preserving atomic spins during collisions [145,236].

Advances in technology have driven efforts to fabricate smaller vapor cells using techniques like silicon micromachining [100,200], anodic bonding [236], and microelectromechanical-based systems (MEMS) [98], addressing challenges related to size, power consumption, and integration into compact systems. These efforts pave the way toward developing millimeter-scale alkali-metal vapor cell technology, enabling devices such as chip-scale atomic clocks [170]. A detailed fabrication process can be found in the comprehensive review of chip-scale atomic devices by John Kitching [79]. Straessle et al. [240] have studied a microfabricated alkali vapor cell with octadecyltrichlorosilane (OTS) anti-relaxation coating using low-temperature indium-bonding [240]. They carried out optical and microwave spectroscopy (double resonance) on the wall-coated cell to evaluate its relaxation properties and potential gas contamination [240]. Their findings validated that cells with coatings achieved lower linewidth than cells without coatings.

Additionally, people have studied cm scale-type cells and microfabricated cells with buffer gases, wall coatings, and wall coatings plus buffer gases. Among these, the best buffer gases are Nitrogen and Argon, while paraffin and OTS are better anti-relaxation coatings. Other avenues with minimal buffer gases plus anti-relaxation coatings could be extensively explored for better clocks.

6.2.1. The Signal Detection System

In vapor cell atomic clocks, the signal detection system comprising the detectors and fluorescence collection optics is pivotal in determining and improving the clock's frequency stability. The different quantum efficiency of detectors and different beam sizes can lead to correspondingly differing values of the light shift effect, although it would not influence the value of the fitted zero-light frequency [187]. Part of the efforts put in place to improve the performance of vapor-cell atomic clocks is particularly for increasing the signal contrast and the atomic line quality factor for optimum signal-to-noise ratio (SNR) [206]. An optimized detection system enhances the SNR, thereby improving the precision of frequency measurements. Hence, the choice of detectors and the design of fluorescence collection optics are crucial for maximizing signal detection efficiency. Large-area photodiodes, while capable of capturing more fluorescence, are susceptible to interference from electronic noise due to the low fluorescence power and the high electronics amplification requisites [160]. This can degrade the SNR and, consequently, the clock's stability. Innovative designs, such as surrounding the vapor cell with curved mirrors to focus fluorescence onto photomultiplier tubes (PMTs), have been shown to significantly enhance signal collection efficiency by up to 200-fold fluorescence capture, as shown by Perrella et al. [160]. This approach not only increases the detected signal but also improves the SNR, leading to better frequency stability by more than 10-fold increase, as well as improved light shift measurement precision [160].

6.3. Density Effects and Impact Due to Spatial Inhomogeneities

Generally, it is well-known that two-photon spectroscopy, including a single-color excitation of Rb 87, is Doppler-free [218,241]. This results from the use of counter-propagating beams that produce narrow transitions, which is efficient due to the intermediate $5P_{3/2}$ state that falls almost halfway between the $5S_{1/2} - 5D_{5/2}$ transition of interest, leading to high signal-to-noise ratios [177]. There is a need to accurately evaluate the dependence of the field strength using the AC Stark effect to

measure transition dipole matrix elements. To experimentally measure the differential polarizability by extracting it from the light shift measurements, a careful understanding of how the light-shift measurement averages over the Gaussian beam intensity profile of the perturbing laser is needed, as well as an accurate account of all transmission losses in the optical beam's path, which is a nontrivial task [214]. Furthermore, spectral features could be misinterpreted by attributing symmetries in resonance lines to the emergence of Autler-Townes-like splitting [242]. This is because the effects of inhomogeneous broadening can produce similar asymmetries, differing primarily in sign, potentially leading to misinterpretation of spectral features [216].

As discussed in [177], and also from Eq.36, in general, the AC Stark shift can be written in SI units as

$$\Delta v(r, z) = \frac{\Delta\alpha}{2c\epsilon_0 h} \langle I(r, z) \rangle, \quad (44)$$

where $\Delta\alpha$ is the differential scalar polarizability of the two clock states (which can be found by summing over electric dipole matrix elements), $I(r, z)$ is the laser's intensity profile (which induces the light shifts), z is the optical axis of the beam, and r is the radial position, h is Planck's constant, c is the speed of light, and ϵ_0 is the permittivity of free space [177].

The atomic vapor density is typically set to attenuate the laser beam by a factor of approximately $1/e$ [119,127], with the light shift more pronounced at the beam's entry point into the cell compared to its exit point, thereby creating a gradient of light shift effects across the cell. In the absence of a light shift, the entire cell maintains a uniform zero-crossing frequency that gets disrupted in the presence of a light shift [127,216,218]. Conducting measurements at multiple light intensities allows for extrapolating the Stark shift to zero intensity [218]. Martin et al. [119] detailed an experimental procedure for estimating this shift. Section 1 below compares different rubidium two-photon and two-color two-photon optical clocks with their reported fractional frequency instabilities, detailing the limiting parameters of light shift, collisional shift, and temperature shift, along with the corresponding clock instabilities. As of the time of this review, to the best of our knowledge, the highest stability attained is 5×10^{-15} at an averaging time of ten days [117]. Martin et al. [119] also reported a value of 7.5×10^{-15} for an averaging time of 1 day. It is to be noted that the key to such performance was having tight control over the laser's power and vapor density. However, reduction of the light shift effect as discussed in section 7 is very much necessary for realizing the best performing clock in long-term.

6.4. Geometrical Broadening

Geometrical broadening refers to the broadening of spectral lines due to the physical geometry and arrangement of the experimental setup, such as the shape of the light beam, the alignment of optical components, or the distribution of atomic or molecular samples. [109,172,218]. Maurice et al. [109] have a detailed characterization of the shift due to optical misalignment, which they suspect to have been caused by the thermal gradients on the aluminum base plate that was used as a stable platform for aligning the optical components. They further recommended suppressing such misalignment of the interrogating beams by using ultra-stable optical assemblies and improved stabilization techniques, which could improve the long-term frequency instability.

6.5. Power Broadening

A high intensity of the interrogating laser can saturate the atomic transition, leading to Power broadening. This saturation is one of the obstructions to higher resolution in two-photon experiments [218]. It can also be caused by population redistribution among the resonant and intermediate levels of the two-photon transition [135], potentially leading to a shift or broadening of the resonance line.

6.6. Second-Order Doppler Effect

As explained by Berquist [218], an oscillating electric field will always induce a second-order energy shift between any pair of levels coupled by an electric dipole interaction, as seen in the AC Stark shift formula (equation (36)). However, if the spectral linewidth is much larger than the second-order shift, the shift remains but is likely insignificant. Hence, if the spectral resolution increases to match or exceed the second-order shift corresponding to the mean thermal velocity, the line shape becomes distorted. Lemke et al. [117] reported a value of $1.35 \times 10^{-15} \text{ K}^{-1}$, while Martin et al [119] reported a value of $1.0 \times 10^{-15} \text{ K}^{-1}$ and Zachary et al. [110] reported the shift as $-1.0 \times 10^{-15} \text{ K}^{-1}$. This shift was reported as negligible in the work of Beard et al. [116].

6.7. Blackbody Radiation (BBR) Shift

At non-zero temperatures, objects emit electromagnetic radiation, which can perturb the atomic energy levels, usually characterized as a BBR shift. The atomic vapor that is immersed in this electromagnetic radiation is usually heated to increase the signal-to-noise ratio [119,243], and the intensity of this shift is determined by the temperature of the vapor cell [117]. At 373 K, Lemke et al. reported a value of $-1.36 \times 10^{-15} \text{ K}^{-1}$, while Martin et al. [119] reported a BBR positive shift of $1.3 \times 10^{-15} \text{ K}^{-1}$, and Zachary et al. [110] reported the shift as $-1.3 \times 10^{-15} \text{ K}^{-1}$. At a temperature of 363.15 K, the scheme by Poulin et al. [120], reported this shift as $-1.37 \times 10^{-15} \text{ K}^{-1}$ and Perrella et al. [122], characterized this shift as $-5.45 \times 10^{-13} \text{ K}^{-1}$ which was higher compared to other reported values. Beard et al. [116] considered this perturbation as negligible in their scheme.

6.8. Atomic Collisions

Atomic collisions within vapor cells, such as Inter-collisions between Rb-Rb atoms, collisions with buffer gases like helium, and the migration of liquid-phase rubidium across the cell windows, significantly contribute to spectral line broadening and frequency shifts in rubidium-based atomic clocks [109,218]. These phenomena lead to density-dependent collisional shifts and reduce the availability of rubidium atoms in the vapor phase, thereby impacting the long-term stability and accuracy of frequency standards. To counteract these effects, several strategies have been employed, such as utilizing a demagnetized multi-layer magnetic shield, which helps mitigate the impacts of magnetic field fluctuations on atomic collision rates and spectral line characteristics. Additionally, adopting helium-impermeable glasses, such as aluminosilicate glasses, for constructing vapor cells effectively reduces helium-induced frequency shifts by preventing helium permeation [117,136]. The Rb-Rb collisional shift can be effectively canceled using a two-photon two-color scheme, which employs different laser frequencies to interact with the rubidium atoms, thus compensating for the shifts induced by collisions [136].

Lemke et al.[117] observed a helium-induced frequency shift with a drift rate of 4×10^{-15} per day alongside a Rb-Rb collision frequency shift of -2930 Hz during a 65-day measurement campaign [117]. Poulin et al. [120] reported an Ar-Rb collisional shift of -703 Hz , while Erickson [171] detailed how helium collisional shifts vary with pressure, quantifying the shift as $5.35 \times 10^{-9} / \text{Torr}$ [171].

While these atomic collisions contribute in a minor way to the overall long-term performance of rubidium frequency standards, their precise quantification and effective mitigation are essential for enhancing the accuracy and reliability of these devices [244].

6.9. DC Stark Shift Contribution

Similar to the AC Stark shift, there is a perturbing effect known as the DC Stark shift – it is the shift in atomic levels due to the presence of an external static electric field [245,246], as discovered in 1913 by J Stark [246]. This shift, which is essentially a limiting case of a low-frequency variable field [246], results from the build-up of charges near the rubidium atoms, say on the vapor cell. Although the shift due to the DC Stark shift does not significantly affect the long-term performance of a clock,

Martin et al. [172] reported a value of $5.9 \times 10^{-15} \text{ V}^2/(\text{cm})^2$ and remarked that a small electric field on the order of 1 V/cm with a slow time wander could, in principle, cause significant long-term instability [172]. Such instability could be eliminated by applying light of sufficient energy (usually a UV LED light) to the surface where the charges have built up to remove the charge [172,247]; this effect is also known as Light Induced Atomic Desorption (LIAD) [248–250]. A careful calculation and estimation of this shift is required to characterize a standard accurately. At the time of this review, only Martin et al. [172] have characterized and reported a value for DC Stark shift. Lemke et al. [117] and Shi et al. [143] reported the shift as negligible in their standard.

7. Methods for Suppressing the Light-Shift Effects

Various experimental methods have been used to reduce light shifts in the rubidium two-photon vapor cell. Given its significant impact, particularly in precision timekeeping, the light shift has attracted extensive research aimed at developing effective suppression techniques. In CPT-based systems, innovative approaches such as the phase jump technique have been utilized to mitigate light shifts. This technique involves forming an error signal in a laser beam with a spatially inhomogeneous intensity profile, stabilizing the amplitude of microwave phase modulation at a value that nullifies the light shift of the CPT resonance [217,251]. Additionally, the implementation of pulsed CPT interrogation within the Ramsey scheme has also shown promise in achieving narrower linewidth and reduced light shift effects [122,148] as studied especially in the cesium vapor cells [148,205,251–253]. In a paraffin-coated cell rubidium frequency standard using double-resonance spectroscopy, light shift reduction has been demonstrated by detuning the laser frequency [215]

Furthermore, various strategies have been tailored for purely optical interrogation methods. These include frequency shifts compensation methods [161], power modulation [252], and the use of dual interrogation techniques [157]. The concept of magic polarization and two-color magic wavelengths have been explored, allowing for cancellation or significant reduction of light shifts in two-photon clocks [72,160], as discussed below.

7.1. Resonance-Offset Locking (ROL)

Resonance-offset locking (ROL) is a novel technique introduced by Li et al. [161] to efficiently compensate for frequency shifts caused by light and vapor-cell variations in atomic clocks. This method leverages the concept of deliberately shifting the locking point away from the peak of the atomic resonance to counteract the frequency deviations induced by environmental changes.

In the ROL approach, an offset is introduced in the locking point based on the measured sensitivity of the atomic signal to changes in vapor-cell temperature and laser power. By selecting an optimal offset voltage, the resonance shifts caused by these environmental factors are neutralized, thereby stabilizing the atomic clock's frequency against external disturbances.

The implementation of this method by Li et al. [161] involved varying the probe light's power and observing the corresponding shifts in the atomic signal amplitude. These shifts are then used to adjust the locking point so that the impact of light and temperature variations on the clock's frequency is minimized. The experiments demonstrated that with an optimal voltage of 25.5 mV, the atomic clock's frequency stability is significantly improved, reducing the susceptibility to light power fluctuations with a linear dependency of $\approx 100 \text{ Hz/mV}$ [161].

This method offers a straightforward and effective solution for enhancing the long-term stability of compact atomic clocks by mitigating two of the most critical sources of frequency instability: light shift and temperature fluctuations. However, it requires careful consideration of the temperature sensitivity of the atomic resonance and the system's overall gain stability, as these factors can influence the effectiveness of the ROL method. While the ROL technique introduces an additional frequency shift that depends on the offset voltage and the amplitude of the atomic resonance, its simplicity and effectiveness in suppressing light shift sensitivity by at least an order of magnitude makes it an

appealing option for compact vapor cell atomic clocks where long-term stability is prioritized over absolute frequency accuracy [161].

7.2. Combined Error Signal Method

The Combined Error Signal (CES) method, developed by Yudin et al. [252], addresses the challenge of suppressing power-induced light shifts in atomic clocks. This innovative technique leverages dual interrogation sequences to enhance clock stability by generating a robust error signal. During each cycle, the laser enables the generation of individual error signals from each interrogation.

These error signals are then combined to form a single, more stable error signal. The CES method achieves this by subtracting these two signals—adjusted by a normalization factor—to correct any frequency shifts caused by the light's power variations. This approach not only stabilizes the clock frequency but also significantly reduces the sensitivity to power fluctuations, improving the overall performance of the system. Further, this technique has shown a tenfold reduction in light shift sensitivity, making it particularly effective for long-term stability in compact atomic clocks [252]. However, this method requires careful consideration of the photodetector gains and the integration of the combined error signals, suggesting areas for further research and optimization.

7.3. Counter-Propagating Beam Approach

The counter-propagating beam approach is an advanced method used to mitigate the effects of light shifts in single-color excitation 778.1 nm, which is advantageous due to its Doppler-free nature. This technique involves the use of a primary laser, tuned to the two-photon transition frequency, and a secondary off-resonance laser, which is precisely tuned to induce a compensatory shift that counteracts the Stark shift caused by the primary laser [172,177].

As described by Martin et al. [172], the primary clock laser operates in resonance with the two-photon transition. Concurrently, an additional Ti:sapphire laser is tuned away from this resonance, with its intensity finely adjusted using a variable optical attenuator. After the lasers are combined, they are routed through a polarization-maintaining fiber splitter — one arm measures the power, while the other directs the beam to the vapor cell, which is regulated by a double-stage temperature control system. The induced frequency shifts are then measured and analyzed using a regression algorithm to ensure precise control [172].

While the two-color, two-photon excitation schemes enhance efficiency in driving the two-photon transition, they introduce complexities such as increased sensitivity to temperature variations and a first-order Doppler shift contribution due to the unequal frequencies of the two lasers [136]. Although this can complicate long-term performance, careful balancing of laser powers, wavelengths, and polarizations can allow for one beam's light to effectively cancel out the other's, as explored in studies by Gerginov et al. and others [118,171,177].

Rhona et al. [177] identified a magic wavelength (a wavelength where there is zero shift of the transition frequency) at 776.179(5) nm for the resonance transition from $5P_{3/2} - 5D_{5/2}$, utilizing two lasers at 1552 nm and 1560 nm, respectively. These are frequency doubled to produce the two-color excitation wavelengths of 776 nm and 780 nm, which are each stabilized to $5S_{1/2}(F = 2) - 5D_{5/2}(F = 4)$ and $5S_{1/2}(F = 2) - 5P_{3/2}(F = 1)$ transitions in Rb, respectively. The combined frequency output, when stabilized, offers a reliable reference against a stable frequency standard. Additionally, a tunable laser introduced into this setup allows for the precise measurement of induced light shifts, further enhancing the robustness of the approach [177]. This counter-propagating beam method, particularly with the incorporation of a magic wavelength and dual interrogation techniques, shows significant promise in reducing the detrimental effects of light shifts on atomic clock performance. However, the complexity of this approach and its dependency on multiple precise adjustments highlight the need for further research, especially to refine the techniques for practical applications and enhance the long-term stability of the clocks.

8. Conclusion and Prospects

This review has analyzed the dominant factors limiting the medium-to-long-term performance of rubidium vapor cell optical clocks, with a little discussion on the Cs two-photon vapor cell optical clock, outlining strategies used by different researchers to minimize the Stark shift (Light Shift effect). Importantly, the natural linewidth of the $6S - 8S$ transition in Cs (1.5 MHz) is larger than the $5S - 5D$ two-photon transition linewidth in Rb (≈ 330 kHz), hence the frequency stability of the laser lock in the Cs transition is certainly not as good as that of Rb [191]. While several authors have proposed different techniques for mitigating the AC Stark shift, their evaluation of the clock's performance is for short or medium-scale performance. The longest measured averaging time remains ten days by Lemke et al. [117] with a light shift value of -4.7×10^{-14} /mW. This value could further improve to the 10^{-15} level by stabilizing the laser power better than $2 \mu\text{W}$ [114,119]. However, unlike the single-color scheme, the studies of light shift effects in the two-color scheme remain experimentally unexplored, especially in a long averaging time period, from a few days to months.

Noteworthy is the potential for significant improvements using novel materials and techniques. For instance, nano-coated or micro-structured surfaces on the inside surface of the vapor cells could help mitigate unwanted collisions, leading to more stable atomic transitions and thereby improved clock stabilities. In addition, leveraging machine learning algorithms to predict and compensate for power and laser frequency drift in real time could drastically improve clock performance and minimize light shift. Recently, efforts have also been channeled toward using an optical frequency comb in building a two-photon optical clock [115]. The performance of the system, both in fractional frequency instability $7.8(35) \times 10^{-15}$ at an averaging time of 2600 s, and the light shift value of 7.6×10^{-12} /mW, is well within comparable limits with conventional excitation using CW lasers as shown in Table 1 [171]. This technique also remains relatively under-explored experimentally, indicating a need for further studies as the broad spectrum available in the direct use of frequency comb has the potential for Doppler background removal, reduced SWaP, and Stark shift mitigation without the need for additional laser systems [115].

The need for a fully automated, portable, and miniaturized optical clock for extra-laboratory use, such as space-related applications, cannot be overemphasized [117,119,135]. Martin et al. pointed out the need to strategically reduce the power consumption of frequency comb [119]. This will help reduce the complexity of the overall clock and contribute to a smaller SWaP. Modern available technologies, such as advances in diode laser systems, should also be applied in investigating the pressure broadening and shift of the Rubidium atom in a two-photon transition for improvements [135,254]. Although significant progress has been made in reducing light shift, there remains a need to efficiently control and mitigate the limitations for reaching the vapor cell optical clock instabilities down to 1×10^{-15} and maintaining it for longer durations up to a week and beyond [86,127]. The techniques covered in this article pave the way for the approaches that one could adopt for reducing the instability-causing parameters in reaching better long-term clock performances.

Author Contributions: A.C.O; formal analysis, data curation, investigation, writing—original draft preparation. B.S; data curation, investigation, review. T.N.B; conceptualization, methodology, validation, writing, review, editing, supervision, and project administration. All authors have read and agreed to the submitted version of the manuscript.

Data Availability Statement: Data sharing does not apply to this article as no new data were created or analyzed in this study.

Acknowledgments: The authors appreciate the University of Alabama College of Arts and Sciences for supporting the Quantime Lab inception and the RA funding for A.C.O. We would like to thank Katie Starliper for proofreading and suggesting the improvements.

Conflicts of Interest: The authors affirm that there is no conflict of interest.

References

- Essen, L.; Parry, J.V. An atomic standard of frequency and time interval: a cesium resonator. *Nature* **1955**, *176*, 280–282.
- Lombardi, M.A. A Historical Review of US Contributions to the Atomic Redefinition of the SI Second in 1967. *Journal of Research of the National Institute of Standards and Technology* **2017**, *122*, 1.
- Ramsey, N.F. History of early atomic clocks. *Metrologia* **2005**, *42*, S1.
- Riley, W.J. A history of the rubidium frequency standard. *IEEE UFFC-S History* **2019**, p. 2.
- Gill, P. When should we change the definition of the second? *Philosophical Transactions of the Royal Society A: Mathematical, Physical and Engineering Sciences* **2011**, *369*, 4109–4130.
- Margolis, H. Optical frequency standards and clocks. *Contemporary Physics* **2010**, *51*, 37–58.
- Aeppli, A.; Kim, K.; Warfield, W.; Safronova, M.S.; Ye, J. Clock with 8×10^{-19} systematic uncertainty. *Physical Review Letters* **2024**, *133*, 023401.
- of Standards, N.I.; Technology. World's most precise and accurate atomic clock pushes new frontiers in Physics. <https://www.nist.gov/news-events/news>.
- Wang, B.; Li, B.; Xiao, Q.; Mo, G.; Cai, Y.F. Space-based optical lattice clocks as gravitational wave detectors in search for new physics. *Science China Physics, Mechanics & Astronomy* **2025**, *68*, 249512.
- Bothwell, T.; Hunt, B.D.; Siegel, J.L.; Hassan, Y.S.; Grogan, T.; Kobayashi, T.; Gibble, K.; Porsev, S.G.; Safronova, M.S.; Brown, R.C.; et al. Lattice Light Shift Evaluations in a Dual-Ensemble Yb Optical Lattice Clock. *Physical Review Letters* **2025**, *134*, 033201.
- Bothwell, T.; Brand, W.; Fasano, R.; Akin, T.; Whalen, J.; Grogan, T.; Chen, Y.J.; Pomponio, M.; Nakamura, T.; Rauf, B.; et al. Deployment of a transportable Yb optical lattice clock. *Optics Letters* **2025**, *50*, 646–649.
- Liao, T.Y.; Liu, H.; Meng, F.; Wang, Q.; Yang, T.; Tian, H.C.; Lu, B.K.; Zhu, L.; Li, Y.; Lin, B.K.; et al. Remote comparison of two Sr optical lattice clocks through a 58 km fiber link. *Chinese Physics Letters* **2025**.
- Shinkai, H.; Takamoto, M.; Katori, H. Transportable optical lattice clocks and general relativity. *arXiv preprint arXiv:2502.06104* **2025**.
- Kale, Y.B.; Singh, A.; Gellesch, M.; Jones, J.M.; Morris, D.; Aldous, M.; Bongs, K.; Singh, Y. Field deployable atomics package for an optical lattice clock. *Quantum Science and Technology* **2022**, *7*, 045004.
- Ohmae, N.; Takamoto, M.; Takahashi, Y.; Kokubun, M.; Araki, K.; Hinton, A.; Ushijima, I.; Muramatsu, T.; Furumiya, T.; Sakai, Y.; et al. Transportable strontium optical lattice clocks operated outside laboratory at the level of 10^{-18} uncertainty. *Advanced Quantum Technologies* **2021**, *4*, 2100015.
- Hobson, R.; Bowden, W.; Vianello, A.; Silva, A.; Baynham, C.F.; Margolis, H.S.; Baird, P.E.; Gill, P.; Hill, I.R. A strontium optical lattice clock with 1×10^{-17} uncertainty and measurement of its absolute frequency. *Metrologia* **2020**, *57*, 065026.
- Kong, D.H.; Wang, Z.H.; Guo, F.; Zhang, Q.; Lu, X.T.; Wang, Y.B.; Chang, H. A transportable optical lattice clock at the National Time Service Center. *Chinese Physics B* **2020**, *29*, 070602.
- Bothwell, T.; Kedar, D.; Oelker, E.; Robinson, J.M.; Bromley, S.L.; Tew, W.L.; Ye, J.; Kennedy, C.J. JILA SrI optical lattice clock with uncertainty of 2.0×10^{-18} . *Metrologia* **2019**, *56*, 065004.
- Bloom, B.; Nicholson, T.; Williams, J.; Campbell, S.; Bishof, M.; Zhang, X.; Zhang, W.; Bromley, S.; Ye, J. An optical lattice clock with accuracy and stability at the 10^{-18} level. *Nature* **2014**, *506*, 71–75.
- Poli, N.; Schioppo, M.; Vogt, S.; Falke, S.; Sterr, U.; Lisdat, C.; Tino, G. A transportable strontium optical lattice clock. *Applied Physics B* **2014**, *117*, 1107–1116.
- Takamoto, M.; Hong, F.L.; Higashi, R.; Katori, H. An optical lattice clock. *Nature* **2005**, *435*, 321–324.
- McGrew, W.; Zhang, X.; Fasano, R.; Schäffer, S.; Beloy, K.; Nicolodi, D.; Brown, R.; Hinkley, N.; Milani, G.; Schioppo, M.; et al. Atomic clock performance enabling geodesy below the centimetre level. *Nature* **2018**, *564*, 87–90.
- Koller, S.; Grotti, J.; Vogt, S.; Al-Masoudi, A.; Dörscher, S.; Häfner, S.; Sterr, U.; Lisdat, C. Transportable optical lattice clock with 7×10^{-17} uncertainty. *Physical review letters* **2017**, *118*, 073601.
- Origlia, S.; Pramod, M.S.; Schiller, S.; Singh, Y.; Bongs, K.; Schwarz, R.; Al-Masoudi, A.; Dörscher, S.; Herbers, S.; Häfner, S.; et al. Towards an optical clock for space: Compact, high-performance optical lattice clock based on bosonic atoms. *Physical Review A* **2018**, *98*, 053443.
- Vogt, S.; Häfner, S.; Grotti, J.; Koller, S.; Al-Masoudi, A.; Sterr, U.; Lisdat, C. A transportable optical lattice clock. In *Proceedings of the Journal of Physics: Conference Series*. IOP Publishing, 2016, Vol. 723, p. 012020.

26. Hausser, H.; Keller, J.; Nordmann, T.; Bhatt, N.; Kiethe, J.; Liu, H.; Richter, I.; von Boehn, M.; Rahm, J.; Weyers, S.; et al. In+ 115-Yb+ 172 Coulomb Crystal Clock with 2.5×10^{-18} Systematic Uncertainty. *Physical Review Letters* **2025**, *134*, 023201.
27. King, S.A.; Spieß, L.J.; Micke, P.; Wilzewski, A.; Leopold, T.; Benkler, E.; Lange, R.; Huntemann, N.; Surzhykov, A.; Yerokhin, V.A.; et al. An optical atomic clock based on a highly charged ion. *Nature* **2022**, *611*, 43–47.
28. Gao, K. The 40Ca+ ion optical clock. *National science review* **2020**, *7*, 1799–1801.
29. Zhang, B.; Huang, Y.; Zhang, H.; Hao, Y.; Zeng, M.; Guan, H.; Gao, K. Progress on the 40Ca+ ion optical clock. *Chinese Physics B* **2020**, *29*, 074209.
30. Diddams, S.A.; Udem, T.; Bergquist, J.; Curtis, E.; Drullinger, R.; Hollberg, L.; Itano, W.M.; Lee, W.; Oates, C.; Vogel, K.; et al. An optical clock based on a single trapped 199Hg+ ion. *Science* **2001**, *293*, 825–828.
31. Zeng, M.; Huang, Y.; Zhang, B.; Hao, Y.; Ma, Z.; Hu, R.; Zhang, H.; Chen, Z.; Wang, M.; Guan, H.; et al. Toward a transportable Ca+ optical clock with a systematic uncertainty of 4.8×10^{-18} . *Physical Review Applied* **2023**, *19*, 064004.
32. Huntemann, N.; Sanner, C.; Lipphardt, B.; Tamm, C.; Peik, E. Single-ion atomic clock with 3×10^{-18} systematic uncertainty. *Physical review letters* **2016**, *116*, 063001.
33. Huang, Y.; Zhang, B.; Zeng, M.; Hao, Y.; Ma, Z.; Zhang, H.; Guan, H.; Chen, Z.; Wang, M.; Gao, K. Liquid-nitrogen-cooled Ca+ optical clock with systematic uncertainty of 3×10^{-18} . *Physical Review Applied* **2022**, *17*, 034041.
34. Marshall, M.C.; Castillo, D.A.R.; Arthur-Dworschack, W.J.; Aeppli, A.; Kim, K.; Lee, D.; Warfield, W.; Hinrichs, J.; Nardelli, N.V.; Fortier, T.M.; et al. High-Stability Single-Ion Clock with 5.5×10^{-19} Systematic Uncertainty. *arXiv preprint arXiv:2504.13071* **2025**.
35. Huntemann, N.; Okhapkin, M.; Lipphardt, B.; Weyers, S.; Tamm, C.; Peik, E. High-accuracy optical clock based on the octupole transition in Yb+ 171. *Physical Review Letters* **2012**, *108*, 090801.
36. Beeks, K.; Sikorsky, T.; Schumm, T.; Thielking, J.; Okhapkin, M.V.; Peik, E. The thorium-229 low-energy isomer and the nuclear clock. *Nature Reviews Physics* **2021**, *3*, 238–248.
37. Kraemer, S.; Moens, J.; Athanasakis-Kaklamanakis, M.; Bara, S.; Beeks, K.; Chhetri, P.; Chrysalidis, K.; Claessens, A.; Cocolios, T.E.; Correia, J.G.; et al. Observation of the radiative decay of the 229Th nuclear clock isomer. *Nature* **2023**, *617*, 706–710.
38. Zhang, C.; von der Wense, L.; Doyle, J.F.; Higgins, J.S.; Ooi, T.; Friebe, H.U.; Ye, J.; Elwell, R.; Terhune, J.; Morgan, H.; et al. 229ThF4 thin films for solid-state nuclear clocks. *Nature* **2024**, *636*, 603–608.
39. Thirolf, P. Shedding Light on the Thorium-229 Nuclear Clock Isomer. *Physics* **2024**, *17*, 71.
40. Scott, J.P.; Potvliege, R.; Carty, D.; Jones, M.P. Trap induced broadening in a potential hydrogen lattice clock. *Metrologia* **2024**, *61*, 025001.
41. Baker, C.; Bertsche, W.; Capra, A.; Carruth, C.; Cesar, C.; Charlton, M.; Christensen, A.; Collister, R.; Mathad, A.C.; Eriksson, S.; et al. Laser cooling of antihydrogen atoms. *Nature* **2021**, *592*, 35–42.
42. Lane, I.C. Production of ultracold hydrogen and deuterium via Doppler-cooled Feshbach molecules. *Physical Review A* **2015**, *92*, 022511.
43. Gabrielse, G.; Glowacz, B.; Grzonka, D.; Hamley, C.; Hessels, E.; Jones, N.; Khatri, G.; Lee, S.; Meisenhelder, C.; Morrison, T.; et al. Lyman- α source for laser cooling antihydrogen. *Optics letters* **2018**, *43*, 2905–2908.
44. Burkley, Z.; Yost, D. Proposal for loading hydrogen into a magic wavelength optical lattice. *Bulletin of the American Physical Society* **2018**, *63*.
45. Liu, Y.; Zhu, X.; Chen, C. Millisecond pulsar augmented atomic clock ensemble timescale algorithm. *Measurement* **2025**, p. 117033.
46. Zheng, Z.H.; Liu, Y.; Shen, D.; Feng, F.; Liu, J.L.; Ma, Y.X.; Zhu, X.W. Research on Pulsar Time Steered Atomic Time Algorithm Based on DPLL. *Research in Astronomy and Astrophysics* **2024**, *24*, 035019.
47. Zhu, X.; Zhang, Z.; Zhao, C.; Li, B.; Tong, M.; Gao, Y.; Yang, T. Research on establishing a joint time-scale of pulsar time and atomic time based on a wavelet analysis method. *Monthly Notices of the Royal Astronomical Society* **2024**, *529*, 1082–1090.
48. Critchley-Marrows, J.; Wu, X.; Ambatali, C.; Nakasuka, S. Pulsar Timing for Clock Stability—Exploring an Autonomous and Resilient Approach to Timing Using Radio Pulsars. In Proceedings of the Proceedings of the 36th International Technical Meeting of the Satellite Division of The Institute of Navigation (ION GNSS+ 2023), 2023, pp. 3175–3189.

49. Hobbs, G.; Guo, L.; Caballero, R.; Coles, W.; Lee, K.; Manchester, R.; Reardon, D.; Matsakis, D.; Tong, M.; Arzoumanian, Z.; et al. A pulsar-based time-scale from the International Pulsar Timing Array. *Monthly Notices of the Royal Astronomical Society* **2020**, *491*, 5951–5965.
50. Taylor, J.H. Millisecond pulsars: Nature's most stable clocks. *Proceedings of the IEEE* **1991**, *79*, 1054–1062.
51. Kim, M. Design and Analysis of High-Stability THz Molecular Clock System. PhD thesis, Massachusetts Institute of Technology, 2022.
52. Leung, K.; Iritani, B.; Tiberi, E.; Majewska, I.; Borkowski, M.; Moszynski, R.; Zelevinsky, T. Terahertz vibrational molecular clock with systematic uncertainty at the 10-14 level. *Physical Review X* **2023**, *13*, 011047.
53. Hanneke, D.; Kuzhan, B.; Lunstad, A. Optical clocks based on molecular vibrations as probes of variation of the proton-to-electron mass ratio. *Quantum Science and Technology* **2020**, *6*, 014005.
54. Roslund, J.D.; Cingöz, A.; Lunden, W.D.; Partridge, G.B.; Kowligy, A.S.; Roller, F.; Sheredy, D.B.; Skulason, G.E.; Song, J.P.; Abo-Shaeer, J.R.; et al. Optical clocks at sea. *Nature* **2024**, *628*, 736–740.
55. Döringshoff, K.; Gutsch, F.B.; Schkolnik, V.; Kürbis, C.; Oswald, M.; Pröbster, B.; Kovalchuk, E.V.; Bawamia, A.; Smol, R.; Schuldt, T.; et al. Iodine frequency reference on a sounding rocket. *Physical Review Applied* **2019**, *11*, 054068.
56. Ye, J.; Ma, L.S.; Hall, J.L. Molecular iodine clock. *Physical review letters* **2001**, *87*, 270801.
57. Day, C. New Accuracy Record for Molecular Lattice Clock. *Physics* **2023**, *16*, 36.
58. Mawdsley, J.P. Terahertz frequency synthesis in CMOS for a chip-scale molecular clock. PhD thesis, Massachusetts Institute of Technology, 2019.
59. Wang, C.; Yi, X.; Mawdsley, J.; Kim, M.; Hu, Z.; Zhang, Y.; Perkins, B.; Han, R. Chip-scale molecular clock. *IEEE Journal of Solid-State Circuits* **2018**, *54*, 914–926.
60. Fortier, T.; Baumann, E. 20 years of developments in optical frequency comb technology and applications. *Communications Physics* **2019**, *2*, 153.
61. Hall, J.L. Optical frequency measurement: 40 years of technology revolutions. *IEEE Journal of Selected Topics in Quantum Electronics* **2000**, *6*, 1136–1144.
62. Sinclair, L.C.; Coddington, I.; Swann, W.C.; Rieker, G.B.; Hati, A.; Iwakuni, K.; Newbury, N.R. Operation of an optically coherent frequency comb outside the metrology lab. *Optics Express* **2014**, *22*, 6996–7006.
63. Jana, S.; Sahoo, B.; Sharma, A. Progress towards the development of a portable all-optical atomic clock based on a two-photon transition in warm atomic vapor. In Proceedings of the 2022 URSI Regional Conference on Radio Science (USRI-RCRS). IEEE, 2022, pp. 1–4.
64. Gill, P. Optical frequency standards. *Metrologia* **2005**, *42*, S125–S137.
65. Bandi, T.N. A comprehensive overview of atomic clocks and their applications. *Demo Journal* **2024**, *1*, 40–50.
66. Strangfeld, A.; Kanthak, S.; Schiemangk, M.; Wiegand, B.; Wicht, A.; Ling, A.; Krutzik, M. Prototype of a compact rubidium-based optical frequency reference for operation on nanosatellites. *Journal of the Optical Society of America B* **2021**, *38*, 1885–1891.
67. Morley, P.D.; Buettner, D.J. *Atomic-Clock Detection of CNO-Based Dark Matter*; IntechOpen, 2024.
68. Safronova, M.; Budker, D.; DeMille, D.; Kimball, D.F.J.; Derevianko, A.; Clark, C.W. Search for new physics with atoms and molecules. *Reviews of Modern Physics* **2018**, *90*, 025008.
69. Dimarcq, N.; Gertsch, M.; Mileti, G.; Bize, S.; Oates, C.; Peik, E.; Calonico, D.; Ido, T.; Tavella, P.; Meynadier, F.; et al. Roadmap towards the redefinition of the second. *Metrologia* **2024**, *61*, 012001.
70. Lodewyck, J. On a definition of the SI second with a set of optical clock transitions. *Metrologia* **2019**, *56*, 055009.
71. Kristen Cote, S.J.; Ryan Zazo, L.M.; Vutha, A.C. The Stratospheric Optical Rubidium Clock Experiment. In Proceedings of the 70th International Astronautical Congress (IAC), Washington D.C., United States, 21-25 October, 2019.
72. Jackson, S.; Vutha, A.C. Magic polarization for cancellation of light shifts in two-photon optical clocks. *Physical Review A* **2019**, *99*, 063422.
73. Riehle, F. Towards a redefinition of the second based on optical atomic clocks. *Comptes Rendus. Physique* **2015**, *16*, 506–515.
74. Yasuda, M.; Inaba, H.; Kohno, T.; Tanabe, T.; Nakajima, Y.; Hosaka, K.; Akamatsu, D.; Onae, A.; Suzuyama, T.; Amemiya, M.; et al. Improved absolute frequency measurement of the ^{171}Yb optical lattice clock towards a candidate for the redefinition of the second. *Applied Physics Express* **2012**, *5*, 102401.

75. McGrew, W.F.; Zhang, X.; Leopardi, H.; Fasano, R.; Nicolodi, D.; Beloy, K.; Yao, J.; Sherman, J.A.; Schaeffer, S.A.; Savory, J.; et al. Towards the optical second: verifying optical clocks at the SI limit. *Optica* **2019**, *6*, 448–454.
76. Yadav, S.; Aswal, D.K. Redefined SI units and their implications. *Mapan* **2020**, *35*, 1–9.
77. Le Targat, R.; Lorini, L.; Le Coq, Y.; Zawada, M.; Guéna, J.; Abgrall, M.; Gurov, M.; Rosenbusch, P.; Rovera, D.; Nagórny, B.; et al. Experimental realization of an optical second with strontium lattice clocks. *Nature communications* **2013**, *4*, 2109.
78. Ludlow, A.D.; Boyd, M.M.; Ye, J.; Peik, E.; Schmidt, P.O. Optical atomic clocks. *Reviews of Modern Physics* **2015**, *87*, 637–701.
79. Kitching, J. Chip-scale atomic devices. *Applied Physics Reviews* **2018**, *5*.
80. Arimondo, E. V coherent population trapping in laser spectroscopy. In *Progress in optics*; Elsevier, 1996; Vol. 35, pp. 257–354.
81. Shah, V.; Kitching, J. Advances in coherent population trapping for atomic clocks. In *Advances in atomic, molecular, and optical physics*; Elsevier, 2010; Vol. 59, pp. 21–74.
82. Petit, G.; Wolf, P.; Delva, P. Atomic time, clocks, and clock comparisons in relativistic spacetime: a review. *Frontiers in relativistic celestial mechanics* **2014**, *2*, 249–279.
83. Kang, S.; Gharavipour, M.; Affolderbach, C.; Gruet, F.; Mileti, G. Demonstration of a high-performance pulsed optically pumped Rb clock based on a compact magnetron-type microwave cavity. *Journal of Applied Physics* **2015**, *117*.
84. Kang, S.; Gharavipour, M.; Gruet, F.; Affolderbach, C.; Mileti, G. Compact and high-performance Rb clock based on pulsed optical pumping for industrial application. In Proceedings of the 2015 Joint Conference of the IEEE International Frequency Control Symposium & the European Frequency and Time Forum. IEEE, 2015, pp. 800–803.
85. Godone, A.; Micalizio, S.; Levi, F. Pulsed optically pumped frequency standard. *Physical Review A—Atomic, Molecular, and Optical Physics* **2004**, *70*, 023409.
86. Gozzelino, M.; Micalizio, S.; Calosso, C.E.; Belfi, J.; Sapia, A.; Gioia, M.; Levi, F. Realization of a pulsed optically pumped Rb clock with a frequency stability below 10⁻¹⁵. *Scientific Reports* **2023**, *13*, 12974.
87. Pei, H.; Pang, H.; Quan, W.; Fan, W.; Yuan, L.; Zhang, K.; Fang, C. Pulsed optical pumping in electron spin vapor. *Measurement* **2024**, *231*, 114619.
88. Hao, Q.; Yang, S.; Zheng, S.; Yun, P.; Ruan, J.; Zhang, S. A 44-cm³ physics package for the high-performance pulsed optically pumped atomic clock. *Review of Scientific Instruments* **2024**, *95*.
89. Hao, Q.; Yang, S.; Ruan, J.; Yun, P.; Zhang, S. Integrated pulsed optically pumped Rb atomic clock with frequency stability of 10⁻¹⁵. *Physical Review Applied* **2024**, *21*, 024003.
90. Micalizio, S.; Levi, F.; Godone, A.; Calosso, C.; Francois, B.; Boudot, R.; Affolderbach, C.; Kang, S.; Gharavipour, M.; Gruet, F.; et al. Pulsed optically pumped Rb clock. In Proceedings of the Journal of Physics: Conference Series. IOP Publishing, 2016, Vol. 723, p. 012015.
91. Micalizio, S.; Godone, A.; Calosso, C.; Levi, F.; Affolderbach, C.; Gruet, F. Pulsed optically pumped rubidium clock with high frequency-stability performance. *IEEE transactions on ultrasonics, ferroelectrics, and frequency control* **2012**, *59*, 457–462.
92. Dong, G.; Deng, J.; Lin, J.; Zhang, S.; Lin, H.; Wang, Y. Recent improvements on the pulsed optically pumped rubidium clock at SIOM. *Chinese Optics Letters* **2017**, *15*, 040201.
93. Shen, Q.; Lin, H.; Deng, J.; Wang, Y. Pulsed optically pumped atomic clock with a medium-to long-term frequency stability of 10⁻¹⁵. *Review of Scientific Instruments* **2020**, *91*.
94. Wang, K.M.; Du, Z.J.; Liu, Y.Y.; Yu, Z.J.; Yan, S.B.; Liu, T.; Dong, R.F.; Zhang, S.G. Pulsed vapor cell atomic clock with a differential Faraday rotation angle detection. *Optics Express* **2021**, *29*, 38527–38539.
95. Baryshev, V.N.; Aleynikov, M.S.; Osipenko, G.V.; Blinov, I.Y. Technique of pulsed optical pumping and pulsed excitation of microwave resonances using the Ramsey scheme in a ⁸⁷Rb cell with a buffer gas. *Quantum Electronics* **2018**, *48*, 443.
96. Choi, I.; Lee, S.; Kwon, T.; Park, S. Improvement of short-term stability of pulsed optically pumped rubidium atomic clock. In Proceedings of the CPEM 2010. IEEE, 2010, pp. 432–433.
97. Lin, H.; Deng, J.; Lin, J.; Zhang, S.; Wang, Y. Frequency stability of a pulsed optically pumped atomic clock with narrow Ramsey linewidth. *Applied Optics* **2018**, *57*, 3056–3060.

98. Knappe, S.; Shah, V.; Schwindt, P.D.; Hollberg, L.; Kitching, J.; Liew, L.A.; Moreland, J. A microfabricated atomic clock. *Applied Physics Letters* **2004**, *85*, 1460–1462.
99. Venkatraman, V.; Kang, S.; Affolderbach, C.; Shea, H.; Mileti, G. Optical pumping in a microfabricated Rb vapor cell using a microfabricated Rb discharge light source. *Applied Physics Letters* **2014**, *104*.
100. Liew, L.A.; Knappe, S.; Moreland, J.; Robinson, H.; Hollberg, L.; Kitching, J. Microfabricated alkali atom vapor cells. *Applied Physics Letters* **2004**, *84*, 2694–2696.
101. Abdullah, S.; Affolderbach, C.; Gruet, F.; Mileti, G. Aging studies on micro-fabricated alkali buffer-gas cells for miniature atomic clocks. *Applied Physics Letters* **2015**, *106*.
102. Nishino, H.; Hara, M.; Yano, Y.; Toda, M.; Kanamori, Y.; Kajita, M.; Ido, T.; Ono, T. A reflection-type vapor cell using anisotropic etching of silicon for micro atomic clocks. *Applied Physics Express* **2019**, *12*, 072012.
103. Maurice, V.; Rutkowski, J.; Kroemer, E.; Bargiel, S.; Passilly, N.; Boudot, R.; Gorecki, C.; Mauri, L.; Moraja, M. Microfabricated vapor cells filled with a cesium dispensing paste for miniature atomic clocks. *Applied Physics Letters* **2017**, *110*.
104. Knappe, S.; Schwindt, P.; Gerginov, V.; Shah, V.; Liew, L.; Moreland, J.; Robinson, H.; Hollberg, L.; Kitching, J. Microfabricated atomic clocks and magnetometers. *Journal of Optics A: Pure and Applied Optics* **2006**, *8*, S318.
105. Kitching, J.; Knappe, S.; Shah, V.; Schwindt, P.; Griffith, C.; Jimenez, R.; Preusser, J.; Liew, L.A.; Moreland, J. Microfabricated atomic magnetometers and applications. In Proceedings of the 2008 IEEE International Frequency Control Symposium. IEEE, 2008, pp. 789–794.
106. HOLLBERG, L.; KITCHING, J. MICROFABRICATED ATOMIC CLOCKS AND MAGNETOMETERS. *LASER SPECTROSCOPY PY*, p. 337.
107. Venkatraman, V.; Pétremand, Y.; de Rooij, N.; Shea, H. Reliability characteristics of microfabricated Rb mini-lamps for optical pumping in miniature atomic clocks and magnetometers. In Proceedings of the Reliability, Packaging, Testing, and Characterization of MOEMS/MEMS and Nanodevices XII. SPIE, 2013, Vol. 8614, pp. 27–33.
108. Carlé, C.; Callejo, M.; Mursa, A.; Hafiz, M.A.; Tanguy, Q.; Vicarini, R.; Millo, J.; Maurice, V.; Klinger, E.; Passilly, N.; et al. Microfabricated vapor cell atomic clocks at FEMTO-ST. In Proceedings of the Hot Vapor Workshop, 2024.
109. Maurice, V.; Newman, Z.L.; Dickerson, S.; Rivers, M.; Hsiao, J.; Greene, P.; Mescher, M.; Kitching, J.; Hummon, M.T.; Johnson, C. Miniaturized optical frequency reference for next-generation portable optical clocks. *Optics Express* **2020**, *28*, 24708–24720.
110. Newman, Z.L.; Maurice, V.; Drake, T.; Stone, J.R.; Briles, T.C.; Spencer, D.T.; Fredrick, C.; Li, Q.; Westly, D.; Ilic, B.R.; et al. Architecture for the photonic integration of an optical atomic clock. *Optica* **2019**, *6*, 680–685.
111. Gellesch, M.; Jones, J.; Barron, R.; Singh, A.; Sun, Q.; Bongs, K.; Singh, Y. Transportable optical atomic clocks for use in out-of-the-lab environments. *Advanced Optical Technologies* **2020**, *9*, 313–325.
112. Takamoto, M.; Ushijima, I.; Ohmae, N.; Yahagi, T.; Kokado, K.; Shinkai, H.; Katori, H. Test of general relativity by a pair of transportable optical lattice clocks. *Nature photonics* **2020**, *14*, 411–415.
113. Grotti, J.; Koller, S.; Vogt, S.; Häfner, S.; Sterr, U.; Lisdat, C.; Denker, H.; Voigt, C.; Timmen, L.; Rolland, A.; et al. Geodesy and metrology with a transportable optical clock. *Nature Physics* **2018**, *14*, 437–441.
114. Callejo, M.; Mursa, A.; Vicarini, R.; Klinger, E.; Tanguy, Q.; Millo, J.; Passilly, N.; Boudot, R. Short-term stability of a microcell optical reference based on the Rb atom two-photon transition at 778 nm. *Journal of the Optical Society of America B* **2024**, *42*, 151–159.
115. Erickson, S.E.; Tooley, D.P.; Weerasinghe, K.; Zhu, X.; Chavez-Pirson, A.; Jason Jones, R. Atomic frequency standard based on direct frequency comb spectroscopy. *Optics Letters* **2024**, *49*, 5340–5343.
116. Beard, R.; Martin, K.W.; Elgin, J.D.; Kasch, B.L.; Krzyzewski, S.P. Two-photon rubidium clock detecting 776 nm fluorescence. *Optics Express* **2024**, *32*, 7417–7425.
117. Lemke, N.D.; Martin, K.W.; Beard, R.; Stuhl, B.K.; Metcalf, A.J.; Elgin, J.D. Measurement of optical rubidium clock frequency spanning 65 days. *Sensors* **2022**, *22*, 1982.
118. Gerginov, V.; Beloy, K. Two-photon optical frequency reference with active ac Stark shift cancellation. *Physical Review Applied* **2018**, *10*, 014031.
119. Martin, K.W.; Phelps, G.; Lemke, N.D.; Bigelow, M.S.; Stuhl, B.; Wojcik, M.; Holt, M.; Coddington, I.; Bishop, M.W.; Burke, J.H. Compact optical atomic clock based on a two-photon transition in rubidium. *Physical Review Applied* **2018**, *9*, 014019.

120. Poulin, M.; Latrasse, C.; Touahri, D.; Têtu, M. Frequency stability of an optical frequency standard at 192.6 THz based on a two-photon transition of rubidium atoms. *Optics Communications* **2002**, *207*, 233–242.
121. Ahern, E.J.; Scholten, S.K.; Locke, C.; Bourbeau-Hebert, N.; White, B.; Luiten, A.N.; Perrella, C. Tailoring the Stability of a Two-Color, Two-Photon Rubidium Frequency Standard. *arXiv preprint arXiv:2410.16654* **2024**.
122. Perrella, C.; Light, P.; Anstie, J.; Baynes, F.; White, R.; Luiten, A. Dichroic two-photon rubidium frequency standard. *Physical Review Applied* **2019**, *12*, 054063.
123. Lab, Q. Tempo Compact Rubidium Optical Clock. <https://quantxlabs.com/wp-content/uploads/2024/09/TEMPO.pdf>.
124. Report, C.Q.C. Infleqtion Sells First Tiqker Quantum Clock in he UK. <https://quantumcomputingreport.com/infleqtion-sells-first-tiqker-quantum-clock-in-the-uk/>.
125. McGuyer, B.H. Atomic physics with vapor-cell clocks. PhD thesis, Princeton University, 2012.
126. Camparo, J. The rubidium atomic clock and basic research. *Physics today* **2007**, *60*, 33–39.
127. McGuyer, B.; Jau, Y.Y.; Happer, W. Simple method of light-shift suppression in optical pumping systems. *Applied Physics Letters* **2009**, *94*.
128. Affolderbach, C.; Breschi, E.; Schori, C.; Mileti, G. Gas-cell atomic clocks for space: new results and alternative schemes. In Proceedings of the International Conference on Space Optics—ICSO 2006. SPIE, 2017, Vol. 10567, pp. 694–700.
129. Göppert-Mayer, M. Über elementarakte mit zwei quantensprüngen. *Annalen der Physik* **1931**, *401*, 273–294.
130. Biraben, F. The first decades of Doppler-free two-photon spectroscopy. *Comptes Rendus. Physique* **2019**, *20*, 671–681.
131. Abella, I. Optical double-photon absorption in cesium vapor. *Physical Review Letters* **1962**, *9*, 453.
132. Roy, R.; Condylis, P.C.; Johnathan, Y.J.; Hessmo, B. Atomic frequency reference at 1033 nm for ytterbium (Yb)-doped fiber lasers and applications exploiting a rubidium (Rb) $5S_{1/2}$ to $4D_{5/2}$ one-colour two-photon transition. *Optics Express* **2017**, *25*, 7960–7969.
133. Khripunov, S.; Radnatarov, D.; Kobtsev, S. Atomic clock based on a coherent population trapping resonance in 87Rb with improved high-frequency modulation parameters. In Proceedings of the Slow Light, Fast Light, and Opto-Atomic Precision Metrology VIII. SPIE, 2015, Vol. 9378, pp. 8–13.
134. Sharma, A.; Kolkowitz, S.; Saffman, M. Analysis of a cesium lattice optical clock. *arXiv preprint arXiv:2203.08708* **2022**.
135. Zamoski, N.D.; Hager, G.D.; Erickson, C.J.; Burke, J.H. Pressure broadening and frequency shift of the $5S_{1/2} - 5D_{5/2}$ and $5S_{1/2} - 7S_{1/2}$ two photon transitions in 85Rb by the noble gases and N_2 . *Journal of Physics B: Atomic, Molecular and Optical Physics* **2014**, *47*, 225205.
136. Nguyen, T.N.; Schibli, T.R. Temperature-shift-suppression scheme for two-photon two-color rubidium vapor clocks. *Physical Review A* **2022**, *106*, 053104.
137. Hassanin, K.; Federsel, P.; Karlewski, F.; Zimmermann, C. $5S - 5D$ two-photon transition in rubidium vapor at high densities. *Physical Review A* **2023**, *107*, 043104.
138. Nez, F.; Biraben, F.; Felder, R.; Millerioux, Y. Optical frequency determination of the hyperfine components of the $5S_{1/2} - 5D_{3/2}$ two-photon transitions in rubidium. *Optics communications* **1993**, *102*, 432–438.
139. Kiran Kumar, P.; Suryanarayana, M. Precision two-photon spectroscopy of alkali elements. *Pramana* **2014**, *83*, 189–219.
140. Martin, K.W.; Lemke, N.D.; Phelps, G.; Burke, J.H.; Stuhl, B. The Optical Stark Shift on a Two-Photon Transition in Rubidium. In Proceedings of the 2018 IEEE International Frequency Control Symposium (IFCS). IEEE, 2018, pp. 1–2.
141. Nguyen, T.N. Degenerate and Non-Degenerate Two-Photon Rubidium Frequency Standard. PhD thesis, University of Colorado at Boulder, 2024.
142. Gusching, A.; Petersen, M.; Passilly, N.; Brazhnikov, D.; Abdel Hafiz, M.; Boudot, R. Short-term stability of Cs microcell-stabilized lasers using dual-frequency sub-Doppler spectroscopy. *Journal of the Optical Society of America B* **2021**, *38*, 3254–3260.
143. Shi, T.; Wei, Q.; Qin, X.; Liu, Z.; Chen, K.; Cao, S.; Shi, H.; Liu, Z.; Chen, J. Dual-frequency optical-microwave atomic clocks based on cesium atoms. *Photonics Research* **2024**, *12*, 1972–1980.
144. Kitching, J.; Knappe, S.; Hollberg, L. Miniature vapor-cell atomic-frequency references. *Applied physics letters* **2002**, *81*, 553–555.
145. Kazakov, G.; Matisov, B.; Litvinov, A.; Mazets, I. Coherent population trapping in a finite-size buffer-less cell. *Journal of Physics B: Atomic, Molecular and Optical Physics* **2007**, *40*, 3851.

146. Erhard, M.; Helm, H. Buffer-gas effects on dark resonances: Theory and experiment. *Physical Review A* **2001**, *63*, 043813.
147. Khan, S.; Kumar, M.P.; Bharti, V.; Natarajan, V. Coherent population trapping (CPT) versus electromagnetically induced transparency (EIT). *The European Physical Journal D* **2017**, *71*, 1–9.
148. Batori, E.; Affolderbach, C.; Pellaton, M.; Gruet, F.; Violetti, M.; Su, Y.; Skrivervik, A.K.; Milet, G. μ POP clock: A microcell atomic clock based on a double-resonance Ramsey scheme. *Physical Review Applied* **2022**, *18*, 054039.
149. Knappe, S.; Schwindt, P.; Shah, V.; Hollberg, L.; Kitching, J.; Liew, L.; Moreland, J. A chip-scale atomic clock based on ^{87}Rb with improved frequency stability. *Optics express* **2005**, *13*, 1249–1253.
150. Bandi, T.; Affolderbach, C.; Stefanucci, C.; Merli, F.; Skrivervik, A.K.; Milet, G. Compact high-performance continuous-wave double-resonance rubidium standard with $1.4 \times 10^{-13} \tau^{-1/2}$ stability. *IEEE transactions on ultrasonics, ferroelectrics, and frequency control* **2014**, *61*, 1769–1778.
151. Gharavipour, M.; Affolderbach, C.; Kang, S.; Bandi, T.; Gruet, F.; Pellaton, M.; Milet, G. High performance vapour-cell frequency standards. In Proceedings of the Journal of Physics: Conference Series. IOP Publishing, 2016, Vol. 723, p. 012006.
152. Affolderbach, C.; Droz, F.; Milet, G. Experimental demonstration of a compact and high-performance laser-pumped rubidium gas cell atomic frequency standard. *IEEE Transactions on Instrumentation and Measurement* **2006**, *55*, 429–435.
153. Chen, K.H.; Wu, C.M.; Wu, S.R.; Yu, H.H.; Liu, T.W.; Cheng, W.Y. Influence of atmospheric helium on secondary clocks. *Optics Letters* **2020**, *45*, 4088–4091.
154. Moreno, W. Rubidium Vapour-cell Frequency Standards: Metrology of Optical and Microwave Frequency References. PhD thesis, Université de Neuchâtel, 2019.
155. Terra, O.; Hussein, H. An ultra-stable optical frequency standard for telecommunication purposes based upon the $5S_{1/2} - 5D_{5/2}$ two-photon transition in Rubidium. *Applied Physics B* **2016**, *122*, 1–12.
156. Martin, K.W. Compact Optical Frequency Standards for Future Applications beyond the Laboratory. PhD thesis, The University of New Mexico, 2019.
157. Li, D.; Liu, K.; Wang, P.; Kang, S. Dual-interrogation method for suppressing light shift in Rb 778 nm two-photon transition optical frequency standard. *Optics Express* **2024**, *32*, 2766–2773.
158. Edwards, C.; Barwood, G.; Margolis, H.; Gill, P.; Rowley, W. Development and absolute frequency measurement of a pair of 778 nm two-photon rubidium standards. *Metrologia* **2005**, *42*, 464.
159. Newman, Z.L.; Maurice, V.; Fredrick, C.; Fortier, T.; Leopardi, H.; Hollberg, L.; Diddams, S.A.; Kitching, J.; Hummon, M.T. High-performance, compact optical standard. *Optics Letters* **2021**, *46*, 4702–4705.
160. Perrella, C. Demonstration of a Two-Photon Atomic Clock with Light Shift Suppression using Two-Colour Magic Wavelengths. Technical report, The University of Adelaide North Terrace, SA, 5005 AUS, 2022.
161. Li, D.; Liu, K.; Zhao, L.; Kang, S. A frequency shift compensation method for light shift and vapor-cell temperature shift in atomic clocks. *arXiv preprint arXiv:2405.14281* **2024**.
162. Plocki, A.; Nguyen, T.N.; Schibli, T. Two-color Rubidium clock with AC Stark Shift Suppression. *Bulletin of the American Physical Society* **2023**.
163. Phelps, G.; Lemke, N.; Erickson, C.; Burke, J.; Martin, K. Compact optical clock with 5×10^{-13} instability at 1 s. *Navigation: Journal of The Institute of Navigation* **2018**, *65*, 49–54.
164. Olson, A.J.; Carlson, E.J.; Mayer, S.K. Two-photon spectroscopy of rubidium using a grating-feedback diode laser. *American Journal of Physics* **2006**, *74*, 218–223.
165. Bigelow, M.S.; Martin, K.W.; Phelps, G.; Lemke, N.D. A high performance clock laser for two-photon frequency stabilized optical clocks. In Proceedings of the CLEO: Science and Innovations. Optica Publishing Group, 2018, pp. JW2A–163.
166. Manurkar, P.; Perez, E.F.; Hickstein, D.D.; Carlson, D.R.; Chiles, J.; Westly, D.A.; Baumann, E.; Diddams, S.A.; Newbury, N.R.; Srinivasan, K.; et al. Fully self-referenced frequency comb consuming 5 watts of electrical power. *OSA Continuum* **2018**, *1*, 274–282.
167. Xu, D.R., June 2022. White Paper: Non-linear Optical Crystals Used for Quantum Technology.
168. Terra, O. Architecture for the photonic integration of an optical atomic clock: supplementary material. *Optica* **2019**, *144*, 83–87.
169. Nikogosyan, D.N. *Nonlinear optical crystals: a complete survey*; Springer Science & Business Media, 2006.

170. Cutler, T.F.; Hamlyn, W.J.; Renger, J.; Whittaker, K.A.; Pizzey, D.; Hughes, I.G.; Sandoghdar, V.; Adams, C.S. Nanostructured alkali-metal vapor cells. *Physical Review Applied* **2020**, *14*, 034054.
171. Erickson, S.E. An Optical Atomic Clock Based on Frequency Comb Spectroscopy. PhD thesis, The University of Arizona, 2024.
172. Martin, K.W.; Stuhl, B.; Eugenio, J.; Safronova, M.S.; Phelps, G.; Burke, J.H.; Lemke, N.D. Frequency shifts due to Stark effects on a rubidium two-photon transition. *Physical Review A* **2019**, *100*, 023417.
173. Bjorkholm, J.; Liao, P. Line shape and strength of two-photon absorption in an atomic vapor with a resonant or nearly resonant intermediate state. *Physical Review A* **1976**, *14*, 751.
174. Egidi, A.; et al. Review of main optical retroreflectors. *Istituto Nazionale di Ricerca Metrologica, Turin, Italy, Tech. Rep. RT 31* **2018**, *31*, 2018. <https://doi.org/10.13140/RG.2.2.12150.04166>.
175. Mungan, C. The cat's Eye Retroreflector. Technical report, United States Naval Academy, Spring 2001.
176. Snyder, J. Paraxial ray analysis of a cat's-eye retroreflector. *Applied optics* **1975**, *14*, 1825–1828.
177. Hamilton, R.; Roberts, B.M.; Scholten, S.K.; Locke, C.; Luiten, A.N.; Ginges, J.S.; Perrella, C. Experimental and Theoretical Study of Dynamic Polarizabilities in the $5S\ 1/2-5D\ 5/2$ Clock Transition in Rubidium-87 and Determination of Electric Dipole Matrix Elements. *Physical Review Applied* **2023**, *19*, 054059.
178. Hilico, L.; Felder, R.; Touahri, D.; Acef, O.; Clairon, A.; Biraben, F. Metrological features of the rubidium two-photon standards of the BNM-LPTF and Kastler Brossel Laboratories. *The European Physical Journal-Applied Physics* **1998**, *4*, 219–225.
179. NEWMAN, Z.L.; MAURICE, V.; DRAKE, T.; STONE, J.R.; BRILES, T.C.; SPENCER, D.T.; FREDRICK, C.; LI, Q.; WESTLY, D.; ILIC, B.; et al. Architecture for the photonic integration of an optical atomic clock: supplementary material. *Optica* **2019**.
180. True, T.M.; Pitz, G.A.; Rice, C.A.; Perram, G.P. Resonant enhancement of two-photon absorption in rubidium with crossed polarizations. *Optics Communications* **2022**, *510*, 127943.
181. Perrella, C.; Light, P.; Anstie, J.; Baynes, F.; Benabid, F.; Luiten, A.N. Two-color rubidium fiber frequency standard. *Optics Letters* **2013**, *38*, 2122–2124.
182. Locke, C.; Ng, S.; Scarabel, J.; O'Connor, M.; Luiten, A.; Scholten, S.; Ahern, E.; Hebert, N.; Perrella, C. Portable Optical Atomic Clock Based on a Dichroic Two-Photon Transition in Rubidium. In Proceedings of the 2023 Joint Conference of the European Frequency and Time Forum and IEEE International Frequency Control Symposium (EFTF/IFCS). IEEE, 2023, pp. 1–2.
183. Miao, J.; Chen, J.; Yu, D.; Yang, Q.; Pan, D.; Chen, J. Single-Atomic-Ensemble Dual-Wavelength Optical Standard. *arXiv preprint arXiv:2411.02107* **2024**.
184. Kulatunga, P.; Busch, H.; Andrews, L.; Sukenik, C. Two-color polarization spectroscopy of rubidium. *Optics Communications* **2012**, *285*, 2851–2853.
185. Caracas Núñez, M.; Gonzalez, M.A.; Núñez Portela, M. Theoretical and experimental study of the $6S-8S$ two-photon absorption cross-section in cesium atoms. *Optics Express* **2023**, *31*, 31749–31759.
186. Uehara, T.; Sugiyama, K.; Kitano, M. Frequency measurement of the $6S-8S$ two-photon transition in cesium. In Proceedings of the Conference on Lasers and Electro-Optics/Pacific Rim. Optica Publishing Group, 2013, p. WPF.3.
187. Wu, C.M.; Liu, T.W.; Wu, M.H.; Lee, R.K.; Cheng, W.Y. Absolute frequency of cesium $6S-8S\ 822\text{ nm}$ two-photon transition by a high-resolution scheme. *Optics letters* **2013**, *38*, 3186–3189.
188. Chen, Y.H.; Liu, T.W.; Wu, C.M.; Lee, C.C.; Lee, C.K.; Cheng, W.Y. High-resolution $Cs\ 133\ 6S-6D, 6S-8S$ two-photon spectroscopy using an intracavity scheme. *Optics letters* **2011**, *36*, 76–78.
189. Wu, C.M.; Cheng, W.Y.; Lee, R.K.; et al. Cesium $6S\ 1/2 \rightarrow 8S\ 1/2$ two photon-transition stabilized 822.5 nm diode laser. In Proceedings of the 2008 Conference on Precision Electromagnetic Measurements Digest. IEEE, 2008, pp. 318–319.
190. Cheng, C.Y.; Wu, C.M.; Liao, G.B.; Cheng, W.Y. Cesium $6S\ 1/2 \rightarrow 8S\ 1/2$ two-photon-transition-stabilized 822.5 nm diode laser. *Optics letters* **2007**, *32*, 563–565.
191. Hagel, G.; Nesi, C.; Jozefowski, L.; Schwob, C.; Nez, F.; Biraben, F. Accurate measurement of the frequency of the $6S-8S$ two-photon transitions in cesium. *Optics communications* **1999**, *160*, 1–4.
192. Lee, Y.C.; Chui, H.C.; Chen, Y.Y.; Chang, Y.H.; Tsai, C.C. Effects of light on cesium $6S-8S$ two-photon transition. *Optics communications* **2010**, *283*, 1788–1791.
193. Sieradzan, A.; Havey, M.; Safronova, M. Combined experimental and theoretical study of the $6p\ 2P\ j \rightarrow 8s\ 2S\ 1/2$ relative transition matrix elements in atomic Cs. *Physical Review A* **2004**, *69*, 022502.

194. Kim, K.t.; Ahn, J. Direct frequency-comb spectroscopy of $6S_{1/2}$ - $8S_{1/2}$ transitions of atomic cesium. *arXiv preprint arXiv:1707.06424* **2017**.
195. Fendel, P.; Bergeson, S.; Udem, T.; Hänsch, T. Two-photon frequency comb spectroscopy of the $6s$ - $8s$ transition in cesium. *Optics letters* **2007**, *32*, 701–703.
196. Bertinetto, F.; Cordiale, P.; Galzerano, G.; Bava, E. Frequency stabilization of DBR diode laser against Cs absorption lines at 852 nm using the modulation transfer method. *IEEE Transactions on Instrumentation and Measurement* **2001**, *50*, 490–492.
197. Nakazawa, M.; Suzuki, K. Cesium optical atomic clock: an optical pulse that tells the time. *Optics Letters* **2001**, *26*, 635–637.
198. Ohtsuka, T.; Nishimiya, N.; Fukuda, T.; Suzuki, M. Doppler-Free Two-Photon Spectroscopy of $6S_{1/2}$ - $2D_{3/2}$ Transition in Cesium. *Journal of the Physical Society of Japan* **2005**, *74*, 2487–2491.
199. Bandi, T.; Affolderbach, C.; Mileti, G. Laser-pumped paraffin-coated cell rubidium frequency standard. *Journal of Applied Physics* **2012**, *111*.
200. Pétremand, Y.; Affolderbach, C.; Straessle, R.; Pellaton, M.; Briand, D.; Mileti, G.; de Rooij, N.F. Microfabricated rubidium vapour cell with a thick glass core for small-scale atomic clock applications. *Journal of Micromechanics and Microengineering* **2012**, *22*, 025013.
201. Knappe, S.; Gerginov, V.; Schwindt, P.; Shah, V.; Robinson, H.; Hollberg, L.; Kitching, J. Atomic vapor cells for chip-scale atomic clocks with improved long-term frequency stability. *Optics letters* **2005**, *30*, 2351–2353.
202. Kazakin, A.; Kleimanov, R.; Komarevtsev, I.; Kondrateva, A.; Enns, Y.; Shashkin, A.; Glukhovskoy, A. Microfabrication of Alkali Vapor MEMS Cells for chip-scale atomic clock. In Proceedings of the Journal of Physics: Conference Series. IOP Publishing, 2021, Vol. 2103, p. 012188.
203. Di Gaetano, E.; Keliehor, B.; Gallacher, K.; Griffin, P.; Sorel, M.; Riis, E.; Paul, D. 778.1 nm distributed feedback lasers for Rb two-photon atomic systems with sub-4 kHz linewidths. *APL Photonics* **2024**, *9*.
204. Hou, D.; Wu, J.; Zhang, S.; Ren, Q.; Zhang, Z.; Zhao, J. A stable frequency comb directly referenced to rubidium electromagnetically induced transparency and two-photon transitions. *Applied Physics Letters* **2014**, *104*.
205. Abdel Hafiz, M.; Carlé, C.; Passilly, N.; Danet, J.; Calosso, C.; Boudot, R. Light-shift mitigation in a microcell-based atomic clock with symmetric auto-balanced Ramsey spectroscopy. *Applied Physics Letters* **2022**, *120*.
206. Lin, J.; Deng, J.; Ma, Y.; He, H.; Wang, Y. Detection of ultrahigh resonance contrast in A_{3B2} show [pmg: line-break justify="yes"/]> vapor-cell atomic clocks. *Optics letters* **2012**, *37*, 5036–5038.
207. Camparo, J.; Frueholz, R. Fundamental stability limits for the diode-laser-pumped rubidium atomic frequency standard. *Journal of applied physics* **1986**, *59*, 3313–3317.
208. Audoin, C.; Candelier, V.; Dimarcq, N. A limit to the frequency stability of passive frequency standards due to an intermodulation effect. *IEEE transactions on instrumentation and measurement* **1991**, *40*, 121–125.
209. Brezinski, M. Noise and system performance with td-oct and sd-oct. *Optical coherence tomography. Academic Press, Burlington* **2006**, pp. 175–195.
210. Duspayev, A.; Owens, C.; Dash, B.; Raithel, G. An optical atomic clock using $4D_{J}$ states of rubidium. *Quantum Science and Technology* **2024**, *9*, 045046.
211. Haas, M.; Jentschura, U.D.; Keitel, C.H. Comparison of classical and second quantized description of the dynamic Stark shift. *American journal of physics* **2006**, *74*, 77–81.
212. Kaplan, A.; Andersen, M.F.; Davidson, N. Suppression of inhomogeneous broadening in rf spectroscopy of optically trapped atoms. *Physical Review A* **2002**, *66*, 045401.
213. Grynberg, G.; Cagnac, B. Doppler-free multiphotonic spectroscopy. *Reports on Progress in Physics* **1977**, *40*, 791.
214. Levi, F.; Camparo, J.; Francois, B.; Calosso, C.; Micalizio, S.; Godone, A. Precision test of the ac Stark shift in a rubidium atomic vapor. *Physical Review A* **2016**, *93*, 023433.
215. Miletic, D.; Bandi, T.; Affolderbach, C.; Mileti, G. ac Stark shift in double resonance and coherent population trapping in a wall-coated cell for compact Rb atomic clocks. *Physica scripta* **2012**, *2012*, 014012.
216. Camparo, J.; Frueholz, R.; Volk, C. Inhomogeneous light shift in alkali-metal atoms. *Physical Review A* **1983**, *27*, 1914.

217. Radnatarov, D.A.; Kobtsev, S.M.; Andryushkov, V.A.; Basalaev, M.Y.; Taichenachev, A.V.; Radchenko, M.D.; Yudin, V.I. Active Suppression of the Light Shift in an Atomic Clock Based on Coherent Population Trapping in 87Rb Vapor Using the Phase Jump Technique. *JETP Letters* **2023**, *117*, 504–508.
218. Bergquist, J.C. Doppler-free spectroscopy. In *Experimental Methods in the Physical Sciences*; Elsevier, 1996; Vol. 29, pp. 255–272.
219. Formichella, V.; Camparo, J.; Tavella, P. Influence of the ac-Stark shift on GPS atomic clock timekeeping. *Applied Physics Letters* **2017**, *110*.
220. Jones, M. Atom-light interactions. **2015**, Archived lecture notes, Durham University.
221. Steck, D.A. Rubidium 87 D line data. Available at <http://steck.us/alkalidata/>.
222. Arora, B.; Safronova, M.; Clark, C.W. Magic wavelengths for the np-ns transitions in alkali-metal atoms. *Physical Review A—Atomic, Molecular, and Optical Physics* **2007**, *76*, 052509.
223. Gallagher, J.; Perram, G. Determining the Two-Photon Absorption Cross-Section for the $5^2S_{1/2} \rightarrow 5^2D_{5/2}$ Transition in Naturally Occurring Rubidium. In Proceedings of the 42nd AIAA Plasmadynamics and Lasers Conference in conjunction with the 18th International Conference on MHD Energy Conversion (ICMHD), 2011, p. 4005.
224. Sakurai, J.; Napolitano, J. *Modern Quantum Mechanics*; Cambridge University Press, 2021.
225. Le Kien, F.; Schneeweiss, P.; Rauschenbeutel, A. Dynamical polarizability of atoms in arbitrary light fields: general theory and application to cesium. *The European Physical Journal D* **2013**, *67*, 1–16.
226. Mitroy, J.a.; Safronova, M.S.; Clark, C.W. Theory and applications of atomic and ionic polarizabilities. *Journal of Physics B: Atomic, Molecular and Optical Physics* **2010**, *43*, 202001.
227. Sheng, D.; Pérez Galván, A.; Orozco, L. Lifetime measurements of the 5 d states of rubidium. *Physical Review A—Atomic, Molecular, and Optical Physics* **2008**, *78*, 062506.
228. Safronova, M.; Williams, C.J.; Clark, C.W. Relativistic many-body calculations of electric-dipole matrix elements, lifetimes, and polarizabilities in rubidium. *Physical Review A* **2004**, *69*, 022509.
229. Wang, X.; Jiang, J.; Xie, L.Y.; Zhang, D.H.; Dong, C.Z. Polarizabilities and tune-out wavelengths of the hyperfine ground states of Rb 87, 85. *Physical Review A* **2016**, *94*, 052510.
230. Di Domenico, G.; Schilt, S.; Thomann, P. Simple approach to the relation between laser frequency noise and laser line shape. *Applied optics* **2010**, *49*, 4801–4807.
231. Zhu, M.; Hall, J.L. Stabilization of optical phase/frequency of a laser system: application to a commercial dye laser with an external stabilizer. *Journal of the Optical Society of America B* **1993**, *10*, 802–816.
232. Camparo, J. Conversion of laser phase noise to amplitude noise in an optically thick vapor. *Journal of the Optical Society of America B* **1998**, *15*, 1177–1186.
233. Drullinger, R.E.; Szekely, C.; Camparo, J.C. Diode-laser-pumped, gas-cell atomic clocks. In Proceedings of the Proceedings of the 1992 IEEE Frequency Control Symposium. IEEE, 1992, pp. 104–107.
234. Robinson, H.; Johnson, C. Narrow 87Rb hyperfine-structure resonances in an evacuated wall-coated cell. *Applied Physics Letters* **1982**, *40*, 771–773.
235. Knappe, S.; Robinson, H.G. Double-resonance lineshapes in a cell with wall coating and buffer gas. *New Journal of Physics* **2010**, *12*, 065021.
236. Seltzer, S.; Michalak, D.; Donaldson, M.; Balabas, M.; Barber, S.; Bernasek, S.; Bouchiat, M.A.; Hexemer, A.; Hibberd, A.; Kimball, D.; et al. Investigation of antirelaxation coatings for alkali-metal vapor cells using surface science techniques. *The Journal of chemical physics* **2010**, *133*.
237. Bandi, T.; Affolderbach, C.; Milet, G. Study of Rb 0-0 hyperfine double-resonance transition in a wall-coated cell. In Proceedings of the EFTF-2010 24th European Frequency and Time Forum. IEEE, 2010, pp. 1–8.
238. Singh, G.; Dilavore, P.; Alley, C.O. A technique for preparing wall coated cesium vapor cells. *Review of Scientific Instruments* **1972**, *43*, 1388–1389.
239. Chu, C.H.; Chang, P.C.; Shih, Y.J.; Luh, D.A.; Chang, M.S.; Liu, T.W.; Lin, Y.T.; Chen, B.W.; Cheng, W.Y. Measurement of the $5S_{1/2}$ to $5D_{5/2}$ two-photon clock transition frequency of rubidium-85 in high vacuum. *Optics Letters* **2023**, *48*, 5984–5987.
240. Straessle, R.; Pellaton, M.; Affolderbach, C.; Pétremand, Y.; Briand, D.; Milet, G.; de Rooij, N.F. Microfabricated alkali vapor cell with anti-relaxation wall coating. *Applied Physics Letters* **2014**, *105*.
241. Stoicheff, B.; Weinberger, E. Doppler-free two-photon absorption spectrum of rubidium. *Canadian Journal of Physics* **1979**, *57*, 2143–2154.

242. Camparo, J. The semiclassical stochastic-field/atom interaction problem. In *Frequency Standards And Metrology*; World Scientific, 2009; pp. 109–117.
243. Kraft, S.; Deninger, A.; Trück, C.; Fortágh, J.; Lison, F.; Zimmermann, C. Rubidium spectroscopy at 778–780 nm with a distributed feedback laser diode. *Laser Physics Letters* **2004**, *2*, 71.
244. Calosso, C.E.; Godone, A.; Levi, F.; Micalizio, S. Enhanced temperature sensitivity in vapor-cell frequency standards. *IEEE transactions on ultrasonics, ferroelectrics, and frequency control* **2012**, *59*, 2646–2654.
245. Mishra, N.S. Frequency modulation of Rydberg states by radio frequency electromagnetic fields. In *Proceedings of the Quantum Sensing and Nano Electronics and Photonics XX*. SPIE, 2024, Vol. 12895, pp. 193–198.
246. Delone, N.B.; Krainov, V.P. AC Stark shift of atomic energy levels. *Physics-Usppekhi* **1999**, *42*, 669.
247. Lodewyck, J.; Bilicki, S.; Bookjans, E.; Robyr, J.L.; Shi, C.; Vallet, G.; Le Targat, R.; Nicolodi, D.; Le Coq, Y.; Guéna, J.; et al. Optical to microwave clock frequency ratios with a nearly continuous strontium optical lattice clock. *Metrologia* **2016**, *53*, 1123.
248. Rebilas, K. Light-induced atomic desorption dynamics: Theory for a completely illuminated cell. *Physical Review A—Atomic, Molecular, and Optical Physics* **2009**, *80*, 014901.
249. Talker, E.; Arora, P.; Zektzer, R.; Sebbag, Y.; Dikopltsev, M.; Levy, U. Light-induced atomic desorption in microfabricated vapor cells for demonstrating quantum optical applications. *Physical Review Applied* **2021**, *15*, L051001.
250. Graf, M.T.; Kimball, D.F.; Rochester, S.M.; Kerner, K.i.; Wong, C.; Budker, D.; Alexandrov, E.B.; Balabas, M.V.; Yashchuk, V.V. Relaxation of atomic polarization in para-n-coated alkali-metal vapor cells. *Physical Review A* **2005**, *72*. <https://doi.org/10.1103/PhysRevA.72.023401>.
251. Yano, Y.; Gao, W.; Goka, S.; Kajita, M. Theoretical and experimental investigation of the light shift in Ramsey coherent population trapping. *Physical Review A* **2014**, *90*, 013826.
252. Yudin, V.; Basalaev, M.Y.; Taichenachev, A.; Pollock, J.; Newman, Z.; Shuker, M.; Hansen, A.; Hummon, M.; Boudot, R.; Donley, E.A.; et al. General methods for suppressing the light shift in atomic clocks using power modulation. *Physical Review Applied* **2020**, *14*, 024001.
253. Abdel Hafiz, M.; Coget, G.; Petersen, M.; Rocher, C.; Guérandel, S.; Zanon-Willette, T.; de Clercq, E.; Boudot, R. Toward a high-stability coherent population trapping Cs vapor-cell atomic clock using autobalanced Ramsey spectroscopy. *Physical Review Applied* **2018**, *9*, 064002.
254. Aumiler, D.; Ban, T.; Pichler, G. High-resolution measurements of the pressure broadening and shift of the rubidium $5S\ 1/2\ 2-6P\ 3/2\ 2$ line by argon and helium. *Physical Review A—Atomic, Molecular, and Optical Physics* **2004**, *70*, 032723.

Disclaimer/Publisher's Note: The statements, opinions and data contained in all publications are solely those of the individual author(s) and contributor(s) and not of MDPI and/or the editor(s). MDPI and/or the editor(s) disclaim responsibility for any injury to people or property resulting from any ideas, methods, instructions or products referred to in the content.